Utrecht University

Master's Thesis

Sedimentation of One and Two Helices including Hydrodynamic Interactions

July 7, 2016

Author:
Barbera Droste

Supervisors:
prof. dr. Marjolein Dijkstra
dr. Joost de Graaf

Universiteit Utrecht

Contents

Chapter 1

Introduction

A colloidal particle moving in a fluid induces a local flow field that affects other particles suspended in the fluid. These interactions are called hydrodynamic interactions (HI), which are long-range, many-body interactions [1]. The interactions with the fluid are known to affect the dynamics of soft matter, e.g. they modify the values of diffusion coefficients [2]. Currently, interest has grown in the study of self-propelling particles. Many examples of self-propelling particles are known from biology such as sperm cells and numerous bacteria. Many bacteria self-propel using one or multiple helical flagella [3, 4].

Much has been written on the fluid dynamics of the helical flagellum. Theoretical models have been employed with the main focus on describing the coupling between the force and torque on a helix and its resulting motion [5, 6]. It is shown that a torque applied on the helix is converted via hydrodynamic friction into translational motion along the helix axis and vice versa [7]. Recent developments in micro swimming robots with applications in located drug delivery in human bodies, have renewed the interest in flagellum-like devices [8]. The self-propulsion of artificial bacterial flagella could be controlled via a low-strength rotating magnetic field [8]. The mobility matrix was estimated experimentally under the light microscope. When the particles were oriented vertically and the magnetic field was switched off, the flagella fell downward in the water due to gravity while rotating around its long axis.
The interest in the self-propulsion is not only of physical interest. To understand the evolution of bacteria and to explain the shape of their helical flagella, the propulsion efficiency of the known shapes was analysed. The helical shape which is most common in nature, corresponds to the largest efficiency [9].
Since hydrodynamic interactions are long-ranged, many-body interactions, finding a solution is in most cases only possible if approximations are made. One of the theories developed to include the effect of hydrodynamic interactions, is slender-body theory. This theory uses the slenderness of the body to approximate the flow field around the body [6]. A comparison between experiments and slender-body theory on a rotating helix at low Reynolds number showed agreement [10].
To understand the self-propulsion of bacteria with multiple flagella, the bundling operation of flagella was already studied in 1976 [11]. Analysis of digital video images of rotating helices shows that the initial rate of bundling is proportional to the motor frequency, when the torque is applied to the top of two helices [12]. For two helices driven by constant torque, their terminal beads fixed in space in harmonic traps, it was numerically shown that their phases synchronise, with a speed decreasing with increasing trap stiffness [13].

Multiple simulation methods have been developed to approximate the hydrodynamic interactions. In 1911 the Stokes flow generated by a point particle in unbounded space was described by Oseen [14]. This tensor was used by Kirkwood in 1954 to compute the hydrodynamic interactions of a chain of molecules [5]. But problems arise when the beads were too close together, the matrix becomes non-positive definite. This is unphysical, since the positivity of diffusion is imposed by the second law of thermodynamics. In 1969 Rotne and Prager modified the Oseen tensor to describe finite sized beads for which the tensor stays positive definite even when the beads overlap [15]. The same expression was obtained by Yamakawa a year later [16]. Their mobility matrix describing the translational coupling between all the beads is called the Rotne-Prager-Yamakawa tensor (RPY). This tensor is one of the most commonly used methods to numerically describe the hydrodynamic interactions between beads. We use a generalisation of

the Rotne-Prager-Yamakawa tensor derived by Wajnryb *et al.* [17] in which also the rotational degrees of freedom are included.

Other methods commonly used are Stokesian Dynamics and lattice-Boltzmann simulations. Stokesian Dynamics (SD) takes into account the lubrication forces, which play a role when the beads are nearly touching [1]. While both the RPY method as the SD method describe the fluid indirectly, lattice-Boltzmann simulations calculate the interactions with the fluid explicitly, although in a simplified manner [18].

As we have discussed above, most research has been done on how an applied torque effects the behaviour of the helix. However, in every system, unless the density of the helix is equal to the fluid in which the particle is suspended, gravity induces a force on the helix. We want to study the effect of the gravitational force on one and two helices, by studying the sedimentation behaviour. For a single helix we are interested to find out how the behaviour is influenced by the thickness of the helix. From bacteria it is known that the helical flagella with which they self-propel, is thin. The ratio between the helical radius and the diameter of the flagella varies between 1/30 to 1/10 [9, 10]. We are interested to find out whether this could have an effect on the behaviour. The sedimentation behaviour is investigated as function of the starting orientation of the helix, and the parameter settings of the helix, such as the aspect ratio and chirality. For two helices, we are interested in their combined behaviour. We want to know how the distance and the initial orientation changes their trajectory. Previous studies on two helices, controlled the distance between them. We are interested to learn what happens if they can freely move.

We find that a single helix suspended in a fluid under the influence of gravity, describes a helical trajectory while spinning around its long axis. The radius and pitch of the trajectory depend on the parameter settings of the helix and the initial orientation. They take values between zero, for which the helix sediments in a straight line, and infinity, for which the helix moves diagonally. The values in between give a helical trajectory. A helical trajectory was predicted as well by the theoretical approach of Dr. A. Morozov. However, the comparison between the theoretical calculations and simulation results shows only limited agreement. It especially fails if the orientation of the helix w.r.t. the xy-plane is varied. Since the comparison with lattice-Boltzmann simulations shows qualitative agreement, this indicates that the theory needs to be adapted to include the time-dependency of the helical axis w.r.t the xy-plane.

For two helices, we find that independent of the initial orientation or distance, the helices almost align with gravity and display a circular movement along their trajectory. The initial conditions determine the trajectory and relative z-position, as well as the relative frequency shift of the two helices.

The outline of this thesis is described below. We will first introduce the relevant parts of the theory of fluid dynamics necessary to study the sedimentation of a helix in low-Reynolds regime in chapter 2. In chapter 3 we will explain the Rotne-Prager-Yamakawa formalism used to model the system. First, we will explain the theoretical expressions and how these can be applied on a rigid object comprised of spheres. Then, we will consider the numerical implementation. At the end of the chapter two other simulation techniques to describe hydrodynamic interactions are briefly explained.
To verify our model, we have compared the sedimentation behaviour of simple rigid bodies to literature. The parametrisations of these bodies, as well as the helix are described in chapter 4. The second part of the chapter discusses the theory for the sedimentation. For the simple bodies, a sphere, dumbbell and L-shape, these are obtained from literature. For the sedimentation of a helix theoretical calculations performed by Dr. A. Morosov based on slender body theory are introduced. Then, the methods used to analyse the trajectory are explained. Finally, the de-dimensionalisation of the simulation is given and the choices for the parameter space are discussed.
Chapter 5 treats the verification of our model. The results for the simple rigid bodies, and the comparison to other simulation techniques and literature are discussed.
Chapter 6 is divided into two sections. The first section examines the results for one helix. It includes a comparison to the theoretical calculations performed by Dr. A. Morozov and lattice-Boltzmann simulation results performed by Dr. J. de Graaf. The second section treats the sedimentation of two helices. The thesis ends with the conclusion, discussion and outlook.

Chapter 2

Hydrodynamic Theory

In this chapter we introduce the relevant parts of the theory of fluid dynamics necessary to study the sedimentation of a helix in low-Reynolds regime.

To fully understand the interactions between the fluid and the colloidal particles, we could investigate the interactions between all fluid molecules and all colloids. That is, examine the change in direction and velocity of all particles in the system for all collisions and then find out fully deterministically the evolution of the system. However, we do not do this, for the following reasons. (i) This would require an infinite amount of computer time, due to the immense amount of fluid particles. (ii) Our predictions could not be tested experimentally, due to the small size of fluid molecules. Fortunately, the size of the fluid molecules is much smaller and their number is much larger than the size and number of the colloids, that a continuum approximation can be made. That is, the fluid can be described as a continuous phase, with a density ρ and flow velocity $\mathbf{u}$, on the order of the length scale of the colloidal particles [2]. We describe this continuum theory next.

Matter cannot be destroyed or created out of nothing. Thus a change in fluid density should be caused by fluid flow, which is described by the Continuity Equation [2]:

$$\frac{\partial \rho(\mathbf{r},t)}{\partial t} = \nabla \cdot (\rho(\mathbf{r},t)\mathbf{u}(\mathbf{r},t)), \tag{2.1}$$

in which $\mathbf{r}$ is the position, t the time, $\rho(\mathbf{r},t)$ the fluid density and $\mathbf{u}(\mathbf{r},t)$ the flow velocity. In the case of an incompressible fluid ($\rho(\mathbf{r},t) \equiv \rho$), which water is to a good approximation [19], this equation reduces to:

$$\nabla \cdot \mathbf{u}(\mathbf{r},t) = 0. \tag{2.2}$$

The colloids and fluid exchange momentum when they interact. If we look at a specific volume, then a change in fluid momentum is caused either by momentum flowing in or out of the surface, or by forces acting on the fluid. These forces can be external forces working on the fluid molecules, such as gravity, or internal forces. The external forces can be described as a change in potential: -$\nabla\Phi$. For the internal forces we have to look at the stress tensor $\boldsymbol{\sigma}$. Its components σ_{ij} describe the force per unit area in direction i through a surface area with normal j. A pressure difference in the fluid creates a net change in momentum perpendicular to the surface of contact. Shear forces, forces which are parallel to the contact area, are caused by a velocity difference in the fluid. Friction between two pieces of liquid with different velocities will cause the slower piece of liquid to gain speed and the faster piece of liquid to lose speed. Combining this means that the internal force, $\mathbf{F}^H$, can be written as [2, 19]:

$$\mathbf{F}^H = \oint_{\partial V} dr^2 \boldsymbol{\sigma} \cdot \mathbf{n} = \int_V dr^3 \nabla \cdot \boldsymbol{\sigma}, \tag{2.3}$$

where we used Gauss' theorem to arrive at the final expression, with V a volume, and ∂V its surface area. As discussed before $\boldsymbol{\sigma}$ is a combination of the hydrodynamic pressure and stress caused by friction. For Newtonian fluids the latter is directly proportional to the gradients of the flow in all directions, $\partial u_i/\partial x_j$

with $i, j \in x, y, z$ [20]. For an isotropic, incompressible fluid this results in:

$$\sigma_{ij} = -p\delta_{ij} + \eta \left(\frac{\partial u_i}{\partial x_j} + \frac{\partial u_j}{\partial x_i} \right), \tag{2.4}$$

with η the dynamic viscosity (kg $\mathrm{m}^{-1}\mathrm{s}^{-1}$). The Navier-Stokes equation for an incompressible, isotropic, Newtonian fluid is then [2]:

$$\rho_m \frac{\partial \mathbf{u}}{\partial t} + \rho_m (\mathbf{u} \cdot \nabla)\mathbf{u} = -\nabla p + \eta \nabla^2 \mathbf{u} - \nabla \Phi \tag{2.5}$$

The Navier-Stokes equation is a non-linear partial differential equation. It is impossible to solve analytically in general. However, there exist reductions which can be made to make the problem more tractable. It is useful to examine whether the flow is dominated by inertia or by viscous forces. The ratio of the inertia and viscous forces is made quantitatively by the Reynolds number [2]:

$$Re = \frac{u^2}{L} / \frac{\eta u}{\rho_m L^2} = \frac{u L \rho_m}{\eta}, \tag{2.6}$$

in which u is the typical flow velocity, L the length scale of the flow, η the viscosity and ρ_m the mass density of the fluid. For colloidal particles in water, L is of the size of the colloids (100 nm), the flow velocity is the thermal velocity of the colloids and plugging in all numbers results in $Re \approx 10^{-3}$.

In the low Reynolds number regime, which we are typically in on the colloidal length scale, the inertia terms in Eq. 2.5 can be ignored. On the time-scale we are interested in, the change in velocity is instantaneous and the colloidal particles are in equilibrium with the surrounding fluid. Therefore the left side of Eq. 2.5 can be neglected. This is called the over-damped regime. Together with the Continuity Equation 2.2 this results in the Stokes equations:

$$-\nabla p - \nabla \Phi + \eta \nabla^2 \mathbf{u} = 0 \tag{2.7}$$

$$\nabla \cdot \mathbf{u} = 0 \tag{2.8}$$

The system is now completely defined by its boundary conditions and potential. Typically, a no-slip at the surface of the particles is imposed, as well as that the flow created by a particle vanishes at infinity.

Chapter 3

The Rotne-Prager-Yamakawa Formalism

In our study we want to model the sedimentation of one and two helices. The helix is built up out of beads of equal radius and distance to calculate the hydrodynamic interactions of a helix with the fluid. With the Rotne-Prager-Yamakawa tensor the hydrodynamic interactions between all the beads can be calculated. In this chapter, we explain the RPY formalism. First, we give the solution of the Stokes equation for a single sphere. Next, we explain how the motion of multiple spheres in a viscous fluid can be approximated using the RPY formalism. The method is subsequently adapted to be applicable to rigid bodies made out of beads. Thereafter the numerical implementation is discussed. Finally, we briefly explain two other hydrodynamic methods, which are used in the verification of the model.

3.1 A Single Sphere in a Fluid

For a single sphere the solution of the Stokes equations is well known. A force $\mathbf{F}$ applied to a sphere causes a sphere to move at constant velocity $\mathbf{u}$, which is given by [2]:

$$\mathbf{u} = \frac{1}{6\pi\eta a}\mathbf{F}. \tag{3.1}$$

A torque $\mathbf{T}$ imposed on a sphere induces a constant angular velocity $\boldsymbol{\omega}$:

$$\boldsymbol{\omega} = \frac{1}{8\pi\eta a^3}\mathbf{T}. \tag{3.2}$$

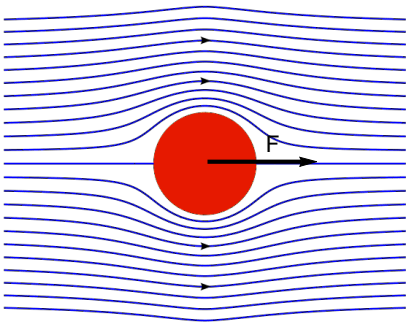

Figure 3.1: Schematic overview of the flow field of a single sphere which is pulled through a fluid [21]. F is the force. The small arrows denote the direction of the flow. The velocity of the sphere is given by Eq. 3.1.

3.2 Interactions between Several Spheres

To approximate the hydrodynamic interactions between two spheres, the Oseen tensor can be used. This tensor describes the flow field due to a point source [17]. To find the translational and rotational flow field generated by a sphere, the Oseen tensor can be integrated over the surface of a sphere. The affect on the velocity of another sphere can be found using Faxen's laws [19] which give an expression for the velocities as function of an external flow. Now a relation is found between the force and torque on one sphere and the translational and angular velocity of another sphere. This two-body hydrodynamic interaction tensor is often referred to as the Rotne-Prager tensor.

Note that the RPY tensor is a far-field approximation, of order $1/r^3$ with r the characteristic particle separation. If the spheres are very close, the approximation breaks down. In reality the second sphere also affects the flow field of the first one, and the analytical expression includes an infinite number of reflections.

For a collection of spheres, hydrodynamics results in many-body interactions, a schematic overview is shown in Fig. 3.2. As a first-order approximation, the many-body interactions can be replaced by two-body interactions. These two-body interactions are collected in matrix form: the RPY tensor. The derivation can be found in [17]. Three-body interactions and higher are neglected in this approach, but that does not affect the order of the approximation, because they only turn up for higher orders [22].

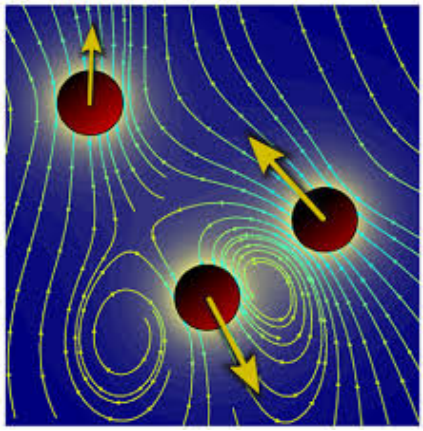

Figure 3.2: Schematic overview of the flow field of three spheres moving through a flowfield [21].

If the forces and torques on the beads are known, the translational and angular velocities can be calculated via:

$$\begin{pmatrix} \mathbf{U}_i \\ \mathbf{\Omega}_i \end{pmatrix} = \sum_{j=1}^{N} \left[\begin{pmatrix} \mu_{ij}^{tt} & \mu_{ij}^{tr} \\ \mu_{ij}^{rt} & \mu_{ij}^{rr} \end{pmatrix} \cdot \begin{pmatrix} \mathbf{F}_j \\ \mathbf{T}_j \end{pmatrix} \right], \tag{3.3}$$

with $\mathbf{U}_i$, $\mathbf{\Omega}_i$ the translational and angular velocity of bead i, N the number of beads, and $\mu_{ij}^{tt}, \mu_{ij}^{rr}, \mu_{ij}^{rt}, \mu_{ij}^{tr}$ the translational-translational, rotational-rotational, rotational-translational and translational-rotational mobility matrices defined as [17]:

$$\mu_{ij}^{tt} = \begin{cases} \dfrac{1}{8\pi\eta R_{ij}} \left[\left(1 + \dfrac{2a^2}{3R_{ij}^2} \right) \mathbb{1} + \left(1 - \dfrac{2a^2}{R_{ij}^2} \right) \hat{\mathbf{R}}_{ij} \hat{\mathbf{R}}_{ij} \right], & R_{ij} > 2a \\ \dfrac{1}{\zeta^{tt}} \left[\left(1 - \dfrac{9R_{ij}}{32a} \right) \mathbb{1} + \dfrac{3R_{ij}}{32a} \hat{\mathbf{R}}_{ij} \hat{\mathbf{R}}_{ij} \right], & R_{ij} \leq 2a \end{cases} \tag{3.4}$$

(3.5)

$$\mu_{ij}^{rr} = \begin{cases} \dfrac{-1}{16\pi\eta R_{ij}^3} \left(\mathbb{1} - 3\hat{\mathbf{R}}_{ij} \hat{\mathbf{R}}_{ij} \right), & R_{ij} > 2a \\ \dfrac{1}{\zeta^{rr}} \left[\left(1 - \dfrac{27R_{ij}}{32a} + \dfrac{5R_{ij}^3}{64a^3} \right) \mathbb{1} + \left(\dfrac{9R_{ij}}{32a} - \dfrac{3R_{ij}^3}{64a^3} \right) \hat{\mathbf{R}}_{ij} \hat{\mathbf{R}}_{ij} \right], & R_{ij} \leq 2a \end{cases} \tag{3.6}$$

(3.7)

$$\mu_{ij}^{rt} = [\mu_{ij}^{tr}]^T = \begin{cases} \dfrac{1}{8\pi\eta R_{ij}^2} \boldsymbol{\epsilon} \cdot \hat{\mathbf{R}}_{ij}, & R_{ij} > 2a \\ \dfrac{1}{16\pi\eta a^2} \left(\dfrac{R_{ij}}{a} - \dfrac{3R_{ij}^2}{8a^2} \right) \boldsymbol{\epsilon} \cdot \hat{\mathbf{R}}_{ij}, & R_{ij} \leq 2a \end{cases} \tag{3.8}$$

with a the radius of the bead, $\zeta^{tt} = 6\pi\eta a$ and $\zeta^{rr} = 8\pi\eta a^3$ the translational and rotational friction coefficients of a single bead, $\mathbf{R}_{ij} = \mathbf{R}_i - \mathbf{R}_j$ the distance vector between beads i and j, $\hat{\mathbf{R}}_{ij}\hat{\mathbf{R}}_{ij}$ the outer product of $\hat{\mathbf{R}}_{ij}$ with itself and

$$\boldsymbol{\epsilon} \cdot \hat{\mathbf{R}}_{ij} = \begin{pmatrix} 0 & \hat{R}_{ij_z} & -\hat{R}_{ij_y} \\ -\hat{R}_{ij_z} & 0 & \hat{R}_{ij_x} \\ \hat{R}_{ij_y} & -\hat{R}_{ij_x} & 0 \end{pmatrix}. \tag{3.9}$$

3.3 Rigid Objects Comprised of RPY Spheres

For any point $\mathbf{R}_{\mathrm{CM}}$ on or outside of a rigid body, the relationship between the forces and torques on all the beads, and the force $\mathbf{F}_{\mathrm{CM}}$ and torque $\mathbf{T}_{\mathrm{CM}}$ on that point are given by[23]:

$$\mathbf{F}_{\mathrm{CM}} = \sum_{i=1}^{N} \mathbf{F}_i, \tag{3.10}$$

$$\mathbf{T}_{\mathrm{CM}} = \sum_{i=1}^{N} [\mathbf{T}_i + (\mathbf{R}_i - \mathbf{R}_{CM}) \times \mathbf{F}_i], \tag{3.11}$$

with $\mathbf{F}_i, \mathbf{T}_i$ the force and torque on sphere i, respectively and $\mathbf{T}_i = \mathbf{R}_i \times \mathbf{F}_i$ the torque on $\mathbf{R}_{\mathrm{CM}}$ due to the force on sphere i.

The relation between $\mathbf{T}_{\mathrm{CM}}$, $\mathbf{F}_{\mathrm{CM}}$ and the torques and forces on the individual beads can be described by a matrix C^T:

$$\begin{pmatrix} \mathbf{F}_{\mathrm{CM}} \\ \mathbf{T}_{\mathrm{CM}} \end{pmatrix} = C^T \begin{pmatrix} \mathbf{F}_1 \\ \vdots \\ \mathbf{F}_N \\ \mathbf{T}_1 \\ \vdots \\ \mathbf{T}_N \end{pmatrix}. \tag{3.12}$$

Using straightforward algebra we find the correct expression for C^T:

$$C^T = \begin{pmatrix} \mathbb{1} & \cdots & \mathbb{1} & \mathbb{0} & \cdots & \mathbb{0} \\ \mathbb{W}_1 & \cdots & \mathbb{W}_N & \mathbb{1} & \cdots & \mathbb{1} \end{pmatrix}, \tag{3.13}$$

with $\mathbb{1}$ the three-dimensional identity matrix, $\mathbb{0}$ the 3×3 zero-matrix and $\mathbb{W}_i$ defined as:

$$\mathbb{W}_i = \begin{pmatrix} 0 & -(R_{i_z} - R_{\mathrm{CM}_z}) & R_{i_y} - R_{\mathrm{CM}_y} \\ R_{i_z} - R_{\mathrm{CM}_z} & 0 & -(R_{i_x} - R_{\mathrm{CM}_x}) \\ -(R_{i_y} - R_{\mathrm{CM}_y}) & R_{i_x} - R_{\mathrm{CM}_x} & 0 \end{pmatrix}. \tag{3.14}$$

In the same way expressions for the translational and angular velocity can be found:

$$\begin{pmatrix} \mathbf{U}_1 \\ \vdots \\ \mathbf{U}_N \\ \boldsymbol{\Omega}_1 \\ \vdots \\ \boldsymbol{\Omega}_N \end{pmatrix} = C \begin{pmatrix} \mathbf{U}_{\mathrm{CM}} \\ \boldsymbol{\Omega}_{\mathrm{CM}} \end{pmatrix}. \tag{3.15}$$

Note that for simplicity we choose $\mathbf{R}_{\mathrm{CM}}$ to be equal to the center of mass, but this is not necessary, the method is precisely the same for any fixed point in the rigid body. To find the friction matrix of the center of mass, ζ_{CM}, we rewrite:

$$\begin{pmatrix} \mathbf{F}_{\mathrm{CM}} \\ \mathbf{T}_{\mathrm{CM}} \end{pmatrix} = C^T \begin{pmatrix} \mathbf{F}_1 \\ \vdots \\ \mathbf{F}_N \\ \mathbf{T}_1 \\ \vdots \\ \mathbf{T}_N \end{pmatrix} = C^T \zeta \begin{pmatrix} \mathbf{U}_1 \\ \vdots \\ \mathbf{U}_N \\ \boldsymbol{\Omega}_1 \\ \vdots \\ \boldsymbol{\Omega}_N \end{pmatrix} = C^T \zeta C \begin{pmatrix} \mathbf{U}_{\mathrm{CM}} \\ \boldsymbol{\Omega}_{\mathrm{CM}} \end{pmatrix}, \tag{3.16}$$

so that

$$\zeta_{CM} = C^T \cdot \zeta \cdot C. \tag{3.17}$$

The mobility matrix of the center of mass is then $\mu_{\text{CM}} = [\zeta_{\text{CM}}]^{-1}$, which can be used to find the translational and angular velocity of the center of mass of the rigid body

$$\begin{pmatrix} \mathbf{U}_{\text{CM}} \\ \mathbf{\Omega}_{\text{CM}} \end{pmatrix} = \mu_{\text{CM}} \begin{pmatrix} \mathbf{F}_{\text{CM}} \\ \mathbf{T}_{\text{CM}} \end{pmatrix}. \tag{3.18}$$

3.3.1 Multiple rigid bodies

In this section, we want to extend the method to multiple rigid bodies. Hence, the grand mobility matrix of the center of masses has to be found, so that we can find the translational and angular velocities of the center of masses:

$$\begin{pmatrix} \mathbf{U}_1^{\text{CM}} \\ \vdots \\ \mathbf{U}_M^{\text{CM}} \\ \mathbf{\Omega}_1^{\text{CM}} \\ \vdots \\ \mathbf{\Omega}_M^{\text{CM}} \end{pmatrix} = \begin{pmatrix} \tilde{\mu}_{11}^{tt} & \dots & \tilde{\mu}_{1M}^{tt} & \tilde{\mu}_{11}^{tr} & \dots & \tilde{\mu}_{1M}^{tr} \\ \vdots & \ddots & \vdots & \vdots & \ddots & \vdots \\ \tilde{\mu}_{M1}^{tt} & \dots & \tilde{\mu}_{MM}^{tt} & \tilde{\mu}_{M1}^{tr} & \dots & \tilde{\mu}_{MM}^{tr} \\ \tilde{\mu}_{11}^{rt} & \dots & \tilde{\mu}_{1M}^{rt} & \tilde{\mu}_{11}^{rr} & \dots & \tilde{\mu}_{1M}^{rr} \\ \vdots & \ddots & \vdots & \vdots & \ddots & \vdots \\ \tilde{\mu}_{M1}^{rt} & \dots & \tilde{\mu}_{MM}^{rt} & \tilde{\mu}_{M1}^{rr} & \dots & \tilde{\mu}_{MM}^{rr} \end{pmatrix} \cdot \begin{pmatrix} \mathbf{F}_1^{\text{CM}} \\ \vdots \\ \mathbf{F}_M^{\text{CM}} \\ \mathbf{T}_1^{\text{CM}} \\ \vdots \\ \mathbf{T}_M^{\text{CM}} \end{pmatrix}, \tag{3.19}$$

with $\mathbf{U}_i^{\text{CM}}$, $\mathbf{\Omega}_i^{\text{CM}}$, $\mathbf{F}_i^{\text{CM}}$, $\mathbf{T}_i^{\text{CM}}$ the translational and angular velocity of the center of mass and force and torque on the center of mass of body i respectively. M the number of rigid bodies, and $\tilde{\mu}_{ij}^{pq}$ the mobility matrix of the center of masses of bodies i and j, $p, q \in r, t$.

To find this mobility matrix we apply almost the same procedure as for one rigid body, only the matrices C and C^T have to be changed to take into account that there are more rigid bodies.

$$\begin{pmatrix} \mathbf{F}_1^{\text{CM}} \\ \vdots \\ \mathbf{F}_M^{\text{CM}} \\ \mathbf{T}_1^{\text{CM}} \\ \vdots \\ \mathbf{T}_M^{\text{CM}} \end{pmatrix} = C^T \begin{pmatrix} \mathbf{F}_1^1 \\ \vdots \\ \mathbf{F}_M^{NB} \\ \mathbf{T}_1^1 \\ \vdots \\ \mathbf{T}_M^{NB} \end{pmatrix}, \tag{3.20}$$

with C^T a $6M \times 6N$ matrix, NB the number of beads per rigid body, $\mathbf{F}_i^j$ and $\mathbf{T}_i^j$ the force and torque on bead j of rigid body i respectively, $i = 1, \dots, M$, $j = 1, \dots, NB$.

$$C^T = \begin{pmatrix} \mathbb{B} & \mathbb{0} & \dots & & & \dots & \mathbb{0} \\ \mathbb{0} & \mathbb{B} & \mathbb{0} & & & & \vdots \\ \vdots & \ddots & \ddots & & & & \\ \mathbb{0} & \dots & \mathbb{0} & \mathbb{B} & \mathbb{0} & & \mathbb{0} \\ \mathbb{W}[1] & \mathbb{0} & & & \mathbb{B} & & \\ \mathbb{0} & \mathbb{W}[2] & \mathbb{0} & & & \ddots & \vdots \\ \vdots & & \ddots & \ddots & & \ddots & \mathbb{0} \\ \mathbb{0} & \dots & \mathbb{0} & \mathbb{W}[M] & \mathbb{0} & & \mathbb{B} \end{pmatrix}, \tag{3.21}$$

with $\mathbb{B}$ a $3\text{NB} \times 3$ matrix $\mathbb{B} = \mathbb{1} \dots \mathbb{1}$ with $\mathbb{1}$ the 3×3 identity matrix, $\mathbb{W}[i] = \mathbb{W}_i^1 \dots \mathbb{W}_i^{NB}$ with $\mathbb{W}_i^j$ defined as:

$$\mathbb{W}_i^j = \begin{pmatrix} 0 & -(R_{i_z}^j - R_{i_z}^{\text{CM}}) & R_{i_y}^j - R_{i_y}^{\text{CM}} \\ R_{i_z}^j - R_{i_z}^{\text{CM}} & 0 & -(R_{i_x}^j - R_{i_x}^{\text{CM}}) \\ -(R_{i_y}^j - R_{i_y}^{\text{CM}}) & R_{i_x}^j - R_{i_x}^{\text{CM}} & 0 \end{pmatrix}. \tag{3.22}$$

With this matrix the same procedure can be used to find the mobility matrix of the center of masses.

3.4 Numerical Implementation

In this section the numerical implementation of the RPY-method is described. The focus is on the implementation for a rigid body. In every section, we briefly describe whether and how this is implemented for independent spheres.

3.4.1 Cholesky decomposition

To invert the $6N \times 6N$ matrices, we use the Armadillo library for C++ [24]. This library makes use of the LAPACK++ library for decompositions of matrices and BLAS for basic linear algebra operations. Because the grand mobility matrix is a positive definite symmetric matrix a Cholesky decomposition is used to find its inverse. Let M be a symmetric, positive definite matrix. Then there is a unique matrix L such that

$$LL^T = M, \tag{3.23}$$

which is called a Cholesky decomposition [25]. L is a lower-triangular matrix. To understand how to find U let us consider one arbitrary element of the (nxn-matrix) M m_{ij}. Because $M = UU^T$

$$m_{ij} = (LL^T)_{ij} = \sum_{k=1}^{k=n} l_{ik} l_{jk} = \sum_{k=1}^{min(i,j)} l_{ik} l_{jk}. \tag{3.24}$$

Since L is a lower-triangular matrix $l_{ij} = 0$ for $1 < i < j < n$ and M is symmetric, so we can calculate $m_{ij} = \sum_{k=1}^{i} l_{ik} l_{jk}$. Rewriting this inductively results in

$$l_{ii} = \sqrt{m_{ii} - \sum_{k=1}^{i-1} l_{ik}^2}, \tag{3.25}$$

$$l_{ij} = \frac{m_{ji} - \sum_{k=1}^{j-1} l_{ik} l_{jk}}{l_{jj}}. \tag{3.26}$$

Now, L can be inverted using back-substitution. The inverse of M is then found by: $M^{-1} = (LL^T)^{-1} = (L^T)^{-1} L^{-1} = (L^{-1})^T L^{-1}$. For independent spheres there is no matrix inversion. Therefore, the inversion procedure is not employed for independent spheres.

3.4.2 Integration procedure

With the mobility tensor(s) found for the center of mass(es), we know how to calculate the velocities and angular velocities of the rigid body, and we want to use this to update its position and orientation. The simplest method to update its center of mass and the spanning vectors $\hat{\boldsymbol{\alpha}}$ and $\hat{\boldsymbol{\beta}}$ would be to use the simple Euler method:

$$\mathbf{R}_{CM_{n+1}} = \mathbf{R}_{CM_n} + \mathbf{u}_n dt, \tag{3.27}$$

$$\hat{\boldsymbol{\alpha}}_{n+1} = \hat{\boldsymbol{\alpha}}_n + \boldsymbol{\omega}_n \times \hat{\boldsymbol{\alpha}}_n dt, \tag{3.28}$$

$$\hat{\boldsymbol{\beta}}_{n+1} = \hat{\boldsymbol{\beta}}_n + \boldsymbol{\omega}_n \times \hat{\boldsymbol{\beta}}_n dt, \tag{3.29}$$

with $\mathbf{u} = \dot{\mathbf{R}}_{CM_i}$ and $\boldsymbol{\omega}_n \times \hat{\boldsymbol{\alpha}}_n = \dot{\boldsymbol{\alpha}}_n$, $\boldsymbol{\omega}_n \times \hat{\boldsymbol{\beta}}_n = \dot{\boldsymbol{\beta}}_n$. But the Euler method is only stable in a small regime [26]. Therefore, we use a fourth order Runge-Kutta integration scheme, which matches the Taylor expansion up to fourth order [26]. This method is widely used, because it is numerically more stable than the Euler method, which is only a first order approximation. It consists of the weighted average of intermediate Euler steps. To update the spanning vector $\hat{\boldsymbol{\alpha}}$ at time step $n+1$, it adds to the vector at time step n the time derivative of alpha $\dot{\boldsymbol{\alpha}}$ times the time step multiplied by a weight, for four intermediate

steps, as is shown in Eq. 3.30.

$$\hat{\boldsymbol{\alpha}}_{n+1} = \hat{\boldsymbol{\alpha}}_n + \frac{dt}{6}(\mathbf{k}_1^{\hat{\boldsymbol{\alpha}}} + 2\mathbf{k}_2^{\hat{\boldsymbol{\alpha}}} + 2\mathbf{k}_3^{\hat{\boldsymbol{\alpha}}} + \mathbf{k}_4^{\alpha}), \tag{3.30}$$

$$\mathbf{k}_1^{\hat{\boldsymbol{\alpha}}} = \dot{\boldsymbol{\alpha}}(\hat{\boldsymbol{\alpha}}_n, \hat{\boldsymbol{\beta}}_n, \mathbf{R}_{CM_n}), \tag{3.31}$$

$$\mathbf{k}_2^{\hat{\boldsymbol{\alpha}}} = \dot{\boldsymbol{\alpha}}(\hat{\boldsymbol{\alpha}}_n + \frac{dt}{2}k_1^{\hat{\boldsymbol{\alpha}}}, \hat{\boldsymbol{\beta}}_n + \frac{dt}{2}\mathbf{k}_1^{\hat{\boldsymbol{\beta}}}, \mathbf{R}_{CM_n} + \frac{dt}{2}\mathbf{k}_1^{\mathbf{R}_{\mathrm{CM}}}), \tag{3.32}$$

$$\mathbf{k}_3^{\hat{\boldsymbol{\alpha}}} = \dot{\boldsymbol{\alpha}}(\hat{\boldsymbol{\alpha}}_n + \frac{dt}{2}k_2^{\hat{\boldsymbol{\alpha}}}, \hat{\boldsymbol{\beta}}_n + \frac{dt}{2}\mathbf{k}_2^{\hat{\boldsymbol{\beta}}}, \mathbf{R}_{CM_n} + \frac{dt}{2}\mathbf{k}_2^{\mathbf{R}_{\mathrm{CM}}}), \tag{3.33}$$

$$\mathbf{k}_4^{\hat{\boldsymbol{\alpha}}} = \dot{\boldsymbol{\alpha}}(\hat{\boldsymbol{\alpha}}_n + dtk_3^{\hat{\boldsymbol{\alpha}}}, \hat{\boldsymbol{\beta}}_n + dt\mathbf{k}_3^{\hat{\boldsymbol{\beta}}}, \mathbf{R}_{CM_n} + dt\mathbf{k}_3^{\mathbf{R}_{\mathrm{CM}}}). \tag{3.34}$$

Independent spheres are defined purely on their center of mass, they do not require spanning vectors. The integration method is thus only dependent on $\mathbf{R}_{CM}$ for $i \in [0, N-1]$.

3.5 Other Hydrodynamic Solvers: Stokesian Dynamics and Lattice Boltzmann

We verify our model by comparing results to two other simulation methods; Stokesian Dynamics and Lattice-Boltzmann. Accordingly, those two methods are briefly explained in this section.

3.5.1 Stokesian Dynamics

A more accurate method we use to verify some of our results, is Stokesian Dynamics. The method is quite similar to the Rotne-Prager-Yamakawa method, but it does not truncate the interactions to the two-body coupling between force-torque and translational-angular velocity, instead it also takes into account the stresslet and strain interactions. This results in an approximation which is of order $1/r^6$ [22]:

$$\begin{pmatrix} \mathbf{U} \\ \mathbf{\Omega} \\ \mathbf{E}^{\infty} \end{pmatrix} = M^{\infty} \begin{pmatrix} \mathbf{F} \\ \mathbf{T} \\ \mathbf{S} \end{pmatrix}, \tag{3.35}$$

with $\mathbf{U}, \mathbf{\Omega}$ the translational and rotational velocity vector of all beads, $\mathbf{E}^{\infty}$ the strain in far-field, $\mathbf{F}, \mathbf{T}, \mathbf{S}$ the force, torque and stress vector respectively, M^{∞} the grand mobility matrix, where the ∞ sign denotes that it is a far-field approximation. The grand mobility matrix is inverted to find the grand resistance matrix R. To this matrix the exact resistance matrix of two spheres at close proximity, R^{2B} is added, and the approximated resistance matrix $R^{2B,\infty} = [M^{2B,\infty}]^{-1}$ is subtracted:

$$R = [M^{\infty}]^{-1} + R^{2B} - R^{2B,\infty}. \tag{3.36}$$

In this way the method accounts for lubrication forces, which are important when two spheres are nearly touching.

3.5.2 Lattice-Boltzmann simulations

The lattice-Boltzmann method explicitly includes the solvent, although at a simplified level. It determines the fluid flow without directly solving the Stokes equation. The LB method can be combined with molecular dynamics simulations to model the behaviour of colloids in a viscous fluid.

The LB method numerically solves the Boltzmann transport equation [18]:

$$\partial_t f(\mathbf{r}, \mathbf{v}, t) + \mathbf{v} \cdot \nabla f(\mathbf{r}, \mathbf{v}, t) = C(f(\mathbf{r}, \mathbf{v}, t). \tag{3.37}$$

This is a time-dependent differential equation for the phase-space probability distribution function $f(\mathbf{r}, \mathbf{v}, t)$, with $\mathbf{r}$ the position, $\mathbf{v}$ the velocity and t the time. The redistribution of the probability distribution due to particle collisions is modelled by a collision operator C. In the LB-method this

equation is discretised. The position of the particles is restricted to a lattice. The velocity is restricted to values which ensure that within one time-step the particles can only move to their neighbouring lattice points. The fluid velocity can then be extracted from the found discrete probability distribution [18].

The method used by Fischer *et al.* [18] to achieve colloid-fluid coupling is by introducing a friction force $\mathbf{F}_d$, which depends on the velocity difference between a colloidal bead and the fluid, scaled by the bare friction coefficient ζ_0:

$$\mathbf{F}_d = -\zeta_0(\mathbf{u}_p - \mathbf{u}_f(\mathbf{r}_p), \tag{3.38}$$

with $\mathbf{u}_p, \mathbf{r}_p$ the particle's velocity and position and $\mathbf{u}_f$ the fluid velocity. Trilinear interpolation is used on the position of the particle to the lattice, because the liquid is only defined on lattice points. An opposite force is applied on the fluid, to conserve momentum.

Chapter 4

Models

The sedimentation behaviour of a helix is the main interest of this thesis. To verify our model, we first investigate simpler rigid bodies, for which we can compare the results with literature. The first section of this chapter introduces the parametrisations of the rigid bodies that we examine: a dumbbell, an L-shape, and a helix. In the second section literature results are introduced for the sedimentation of a dumbbell and L-shaped particle. For helices, we introduce the theoretical expressions based on slender body theory, derived by Dr. A. Morozov, to which we compare our results in Chapter 6. The last section treats the way we analyse the trajectories obtained by the sedimentation of one and two helices and the relevant parameter settings.

4.1 Parametrisations

In this section, we give the parametrisations of the investigated rigid bodies. For all shapes, we first choose a fixed point $\mathbf{R}_{\mathrm{CM}}$ and define a co-moving frame by the axis spanning the body. Let the unit vector $\hat{\boldsymbol{\alpha}}$ correspond with the long axis of the body and $\hat{\boldsymbol{\beta}}$ perpendicular to $\hat{\boldsymbol{\alpha}}$ with the short axis. The third spanning vector is defined by the cross product $\hat{\boldsymbol{\alpha}} \times \hat{\boldsymbol{\beta}}$. Let θ be the angle between $\hat{\boldsymbol{\alpha}}$ and the xy-plane. Then we define $\hat{\boldsymbol{\alpha}} = (0, \cos\theta, \sin\theta)$, $\hat{\boldsymbol{\beta}} = (0, -\sin\theta, \cos\theta)$. An example is shown in Fig. 4.1. The axes are fixed to the body, so when the body rotates, the axes will change accordingly. How their direction is updated, is described in Subsection 3.4.2.

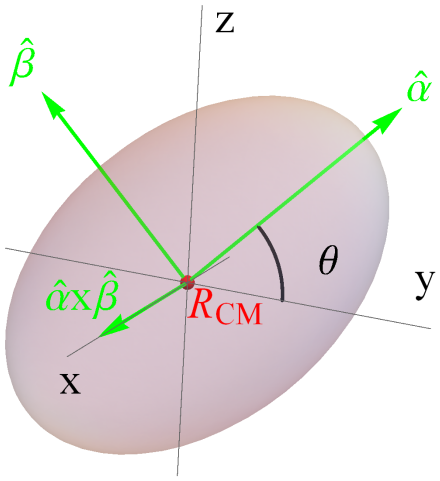

Figure 4.1: Example of the parametrisation of an arbitrary rigid body. The fixed point $\mathbf{R}_{\mathrm{CM}}$ is chosen to be in the center. The three green arrows denote the body axes: $\hat{\boldsymbol{\alpha}}$ corresponds to the long axis of the body, $\hat{\boldsymbol{\beta}}$ and $\hat{\boldsymbol{\alpha}} \times \hat{\boldsymbol{\beta}}$ to the short axes. θ denotes the angle between $\hat{\boldsymbol{\alpha}}$ and the xy-plane.

4.1.1 Dumbbell

A dumbbell consists of two spheres with radii a_1 and a_2 at a fixed distance r. In our simulations the two spheres have the same radius a, the distance between the centres is set such that the beads are touching $r = 2.006a$ to be comparable to the dumbbell studied in [18]. The two sphere centres $\mathbf{R}_j$ of the dumbbell are then positioned at:

$$\mathbf{R}_j = \mathbf{R}_{\mathrm{CM}} + (j - \frac{1}{2})r\hat{\boldsymbol{\alpha}} \tag{4.1}$$

with $j \in \{0, 1\}$ the number of the bead and $\hat{\boldsymbol{\alpha}} = \hat{\mathbf{y}}$, initially.

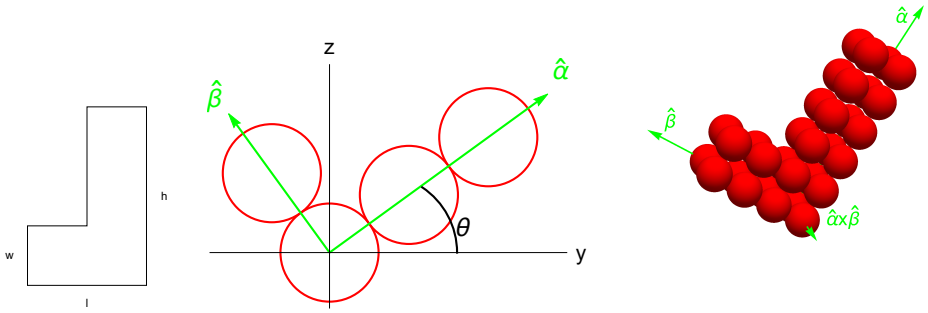

Figure 4.2: Schematic representations of the L-shaped particle. (a) A geometric representation in two dimensions. h is the height, l is the bottom length and w is the width of the shape. (b) A two-dimensional representation of the L-shaped particle for four beads. The beads are shown as red circles, the spanning vectors $\hat{\boldsymbol{\alpha}}$ and $\hat{\boldsymbol{\beta}}$ are shown in green, θ denotes the angle the long axes makes with the y-axis. (c) A three-dimensional representation for 32 beads. The beads are shown as red spheres and the spanning vectors $\hat{\boldsymbol{\alpha}}$, $\hat{\boldsymbol{\beta}}$ and $\hat{\boldsymbol{\alpha}} \times \hat{\boldsymbol{\beta}}$ are shown in green.

4.1.2 L-Shape

First we model the L-shaped particle as a rigid body consisting of 4 beads. We have chosen this number of beads, to have comparable dimensions to the particle used in literature. One of the beads is chosen as fixed point $\mathbf{R}_{\mathrm{CM}}$. Note that it is not the center of mass, but that this is not a problem as our method of simulating rigid bodies is applicable to any fixed point that connects the beads spanning the object. We set the radius, a, of each of the spheres equal to 1 and the distance between the centres of neighbouring beads r is chosen to be $2.01a$:

$$\begin{aligned} \mathbf{R}_0(r) &= \mathbf{R}_{\mathrm{CM}} + r\hat{\boldsymbol{\beta}}, \\ \mathbf{R}_1(r) &= \mathbf{R}_{\mathrm{CM}}, \\ \mathbf{R}_2(r) &= \mathbf{R}_{\mathrm{CM}} + r\hat{\boldsymbol{\alpha}}, \\ \mathbf{R}_3(r) &= \mathbf{R}_{\mathrm{CM}} + 2r\hat{\boldsymbol{\alpha}}, \end{aligned} \tag{4.2}$$

A schematic representation of the model of the L-shape is shown in Fig. 4.2b. We want to investigate whether the number of beads influences the result. Therefore, we also consider a model where the number of beads is 32. For the L-shaped particle consisting of 32 beads, every bead is replaced by a block of 8 beads, compared to the schematic with 4 beads. The first four beads form a square spanned by $\hat{\boldsymbol{\alpha}}$ and $\hat{\boldsymbol{\beta}}$. The last four beads are a copy of this square in the direction perpendicular to the plane $\hat{\boldsymbol{\alpha}} \times \hat{\boldsymbol{\beta}}$:

$$\begin{aligned} \mathbf{R}_i^0 &= \mathbf{R}_i(4.02a), & \mathbf{R}_i^4 &= \mathbf{R}_i^0 + 2.01\hat{\boldsymbol{\alpha}} \times \hat{\boldsymbol{\beta}}, \\ \mathbf{R}_i^1 &= \mathbf{R}_i^0 + 2.01\hat{\boldsymbol{\alpha}}, & \mathbf{R}_i^5 &= \mathbf{R}_i^1 + 2.01\hat{\boldsymbol{\alpha}} \times \hat{\boldsymbol{\beta}}, \\ \mathbf{R}_i^2 &= \mathbf{R}_i^0 + 2.01(\hat{\boldsymbol{\alpha}} + \hat{\boldsymbol{\beta}}), & \mathbf{R}_i^6 &= \mathbf{R}_i^2 + 2.01\hat{\boldsymbol{\alpha}} \times \hat{\boldsymbol{\beta}}, \\ \mathbf{R}_i^3 &= \mathbf{R}_i^0 + 2.01\hat{\boldsymbol{\beta}}, & \mathbf{R}_i^7 &= \mathbf{R}_i^3 + 2.01\hat{\boldsymbol{\alpha}} \times \hat{\boldsymbol{\beta}}, \end{aligned} \tag{4.3}$$

with $\mathbf{R}_i(4.02a)$ defined as before, $i = 0, 1, 2, 3$.

4.1.3 Helix

A helix can be parametrized by its radius r, number of windings w and pitch λ:

$$r\cos\phi\hat{\boldsymbol{\beta}} + r\sin\phi\hat{\boldsymbol{\alpha}} \times \hat{\boldsymbol{\beta}} + \frac{\lambda}{2\pi}\phi\hat{\boldsymbol{\alpha}} \qquad \phi \in [-\pi w, \pi w], \tag{4.4}$$

where $\hat{\boldsymbol{\alpha}}$ and $\hat{\boldsymbol{\beta}}$ are the long and short axis of the helix. The sign of λ determines the chirality of the helix: where $\lambda > 0$ is a right-handed helix (counter-clockwise rotation), and $\lambda < 0$ is a left-handed helix (clockwise-rotation). A schematic representation is shown in Fig. 4.3, where $\hat{\boldsymbol{\alpha}}$ and $\hat{\boldsymbol{\beta}}$ denote the long

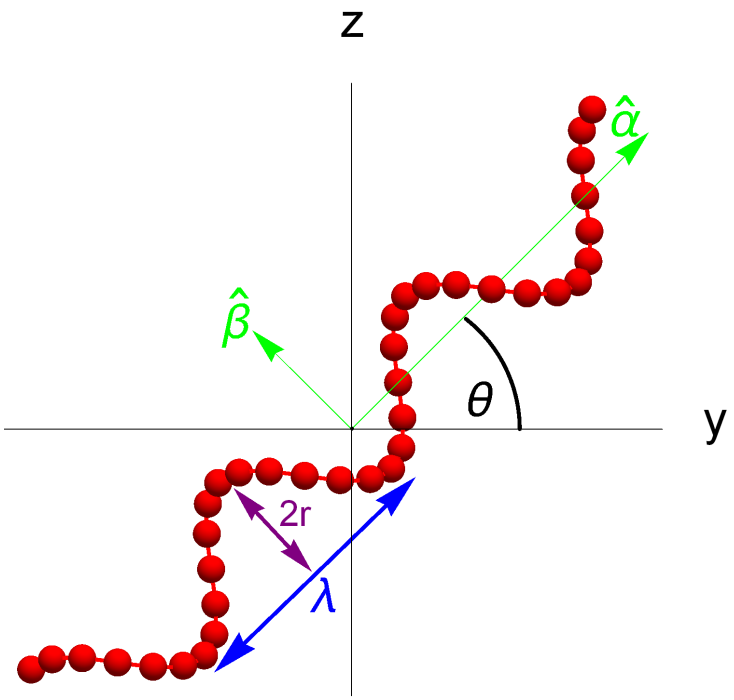

Figure 4.3: Schematic representation of a helix. The main axes of the helix are denoted $\hat{\boldsymbol{\alpha}}$ and $\hat{\boldsymbol{\beta}}$, θ is the angle between the long axis of the helix and the xy-plane, r the radius and λ the pitch. The number of windings shown here is 3.

and short axis of the helix. θ is defined as the angle between the xy-plane and $\hat{\boldsymbol{\alpha}}$. From the figure you already can see that the fixed point $\mathbf{R}_{\mathrm{CM}}$, which is the origin of $\hat{\boldsymbol{\alpha}}$ and $\hat{\boldsymbol{\beta}}$, lays outside the helix.

Using the parametrisation of the helix, the position of the beads can be found by:

$$\mathbf{R}_j = \mathbf{R}_{\mathrm{CM}} + \xi_{1_j}\hat{\boldsymbol{\alpha}} + \xi_{2_j}\hat{\boldsymbol{\beta}} + \xi_{3_j}\hat{\boldsymbol{\alpha}} \times \hat{\boldsymbol{\beta}}, \tag{4.5}$$

$$\xi_{1_j} = \frac{\lambda}{2\pi}\left(\frac{2\pi j}{m} - \frac{\pi}{m}(N-1)\right), \tag{4.6}$$

$$\xi_{2_j} = r\cos\left[\frac{2\pi j}{m}\right], \tag{4.7}$$

$$\xi_{3_j} = r\sin\left[\frac{2\pi j}{m}\right], \tag{4.8}$$

$$\tag{4.9}$$

with r the radius of the helix, λ the pitch, $j \in [0, N-1]$ the bead number, m the number of beads per winding and N the total number of beads.

4.2 Theory for the Sedimentation

For the dumbbell and the L-shape the expected results based on simulations and experiment are presented. Theoretical calculations by dr. A. Morozov on a sedimenting helix are introduced and the predicted sedimentation behaviour is discussed.

Method	$\mu_{\parallel}^{tt}/\mu_0^{tt}$	$\mu_{\perp}^{tt}/\mu_0^{tt}$	$\mu_{\parallel}^{rr}/\mu_0^{rr}$	$\mu_{\perp}^{rr}/\mu_0^{rr}$
Raspberry, filled[18]	0.77 ± 0.01	0.69 ± 0.01	0.55 ± 0.01	0.27 ± 0.01
HYDRO++[27]	0.77 ± 0.01	0.70 ± 0.01	0.55 ± 0.01	0.27 ± 0.01

Table 4.1: Coefficients of the mobility matrix of a dumbbell taken from [18]. **(author?)** [18] compare the results of their Raspberry model and the HYDRO++ program [27]. μ^{tt} and μ^{rr} are the translational-translational and the rotational-rotational mobility matrices. $\perp$ and $\parallel$ denote that the component of the mobility matrix is perpendicular or parallel, respectively, to the long axis of the dumbbell. The results are non-dimensionalised by dividing the components by their corresponding terms for a sphere with the same radius as one of the lobes, μ_0.

4.2.1 Mobility Tensor for a dumbbell

For a dumbbell which has its long axis along $\hat{y}$ the mobility tensor is given by:

$$\mu = \begin{pmatrix} \mu_{\perp}^{tt} & 0 & 0 & 0 & 0 & 0 \\ 0 & \mu_{\parallel}^{tt} & 0 & 0 & 0 & 0 \\ 0 & 0 & \mu_{\perp}^{tt} & 0 & 0 & 0 \\ 0 & 0 & 0 & \mu_{\perp}^{rr} & 0 & 0 \\ 0 & 0 & 0 & 0 & \mu_{\parallel}^{rr} & 0 \\ 0 & 0 & 0 & 0 & 0 & \mu_{\perp}^{rr} \end{pmatrix}. \tag{4.10}$$

In this equation, μ^{tt} and μ^{rr} are the translational-translational and rotational-rotational mobility matrices. $\perp$ and $\parallel$ denote that the component of the mobility matrix is perpendicular or parallel, respectively, to the long axis of the dumbbell. All the cross-coupling terms are zero due to symmetry [18]. We want to compare our method to results obtained by **(author?)** [18]. They used a Raspberry model to calculate these coefficients and compared these with results obtained using the HYDRO++ program [27]. The Raspberry model dumbbell in their method is built up from smaller spheres with radius a. The effective radius of one of the bigger spheres is $3.5a$ and the distance between the two centres is $7a$. They calculated the coefficients for a dumbbell both for which its volume is completely filled with small spheres as well as for which only its surface is covered. We will compare our results to the filled dumbbell, since this gives the best correspondence to the HYDRO++ simulations, as discussed in [18]. The mobility coefficients are non-dimensionalised by dividing them by the translational and rotational mobility matrix for a single sphere of radius $3a$. Their results are shown in Table 4.1.

4.2.2 Sedimentation of an L-Shape

We compare the terminal angle θ_f under which the L-shaped particle sediments without self-propulsion with results obtained by **(author?)** [28]. They experimentally and theoretically studied the behaviour of an sedimenting L-shape for different self-propulsion strengths. The self-propulsion was tuned by a thin gold coating (Au) on the front side of the short arm. When a laser illuminates the particle, this leads to local heating and a local demixing of a sub-critical lutadine suspension, which drives the particle forward. The motion of the particle was restricted to two spatial dimensions by the height of the sample cell. The gravitational strength was tuned by fixing the sample cell at an angle relative to the horizontal plane. They used an L-shaped particle with height $h = 9\mu$m, width $w = 3\mu$m, length $l = 6\mu$m. The dimensions are defined in Fig. 4.2a. The thickness of the particle is equal to the width. Without self-propulsion, they found that the L-shape sediments under a final angle $\theta_f = 56°$, which is the value to which we compare. No difference in the sedimentation angle was observed for particles without a coating, implying that the weight asymmetry due to the gold coating did not effect the sedimentation behaviour. We can therefore safely assume homogeneous mass distribution in our comparison..

4.2.3 Theoretical Calculations for a Helix

To predict the sedimentation behaviour of a helix Dr. A. Morozov of Edinburgh University performed theoretical calculations. He used slender-body theory to find an expression for the translational and angular velocity of the helix, which can be used to find the position of the center of mass as a function of

the time. Here, we briefly describe the method and the assumptions made, and give the expressions found.

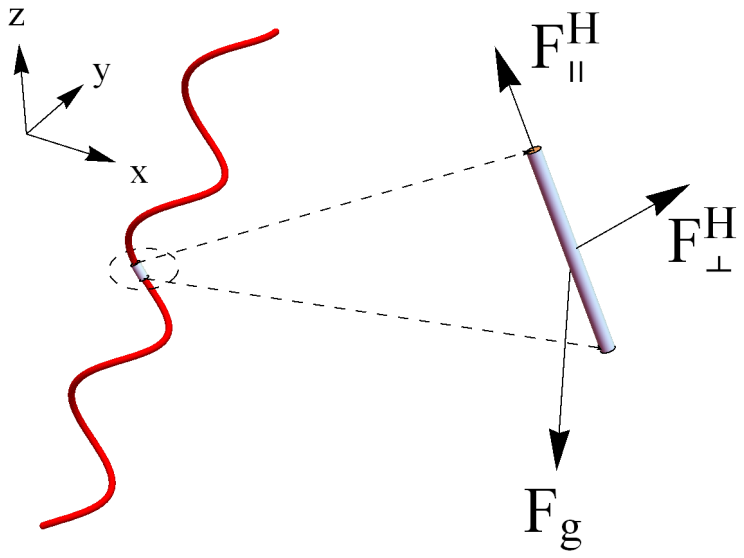

Figure 4.4: Schematic representation of slender body theory applied to a helix. The red helix is divided into small sphero-cylinders, of which one is shown and augmented at the right. The hydrodynamic force F^H is decomposed into components parallel, $F^H_\parallel$, and perpendicular, $F^H_\perp$, to the helix. The gravitational force F_g is directed along $-\hat{z}$.

The helix is divided into pieces of unit length, which can be seen as small sphero-cylinders. In slender body theory the assumption is made that $L \gg D$ with L the length of the segment and D the diameter. On every piece the force due to hydrodynamic interactions must be equal to the gravitational force. This hydrodynamic force is decomposed into components parallel and perpendicular to the helical segment, with corresponding friction coefficients $K_\parallel$ and $K_\perp$:

$$\mathrm{d}\mathbf{F} = -\left(K_\parallel(\mathbf{u}\cdot\mathbf{t})\mathbf{t} + K_\perp(\mathbf{u} - (\mathbf{u}\cdot\mathbf{t})\mathbf{t})\right)\mathrm{d}s \tag{4.11}$$

with $\mathbf{u}$ the velocity of the helix, $\mathbf{t}$ the tangent vector of the helical segment and $\mathrm{d}s$ the segment length. A schematical representation of the forces on the helical segment is shown in Fig. 4.4.

Define $\gamma = K_\perp/K_\parallel$, the ratio of the perpendicular and parallel friction coefficients. The friction coefficients are related to the diffusion coefficients via $K_{\parallel,\perp} = k_BT/D_{\parallel,\perp}$ [29]. We use the analytical expressions for the parallel and perpendicular diffusion coefficient of a sphero-cylinder[30, 31]. In the limit of $p = L/D \to \infty$ γ then becomes:

$$\gamma = \lim_{p\to\infty} 2\frac{\log p - 0.207 + 0.980/p - 0.133/p^2}{\log p + 0.839 + 0.185/p + 0.233/p^2} \tag{4.12}$$

$$= 2. \tag{4.13}$$

The gravitational force induces no torque, but the hydrodynamic force does, which results in an angular

velocity. To simplify the derived expressions let us first introduce some parameters:

$$\chi = \tan^{-1}\left(\frac{2\pi r}{\lambda}\right), \tag{4.14}$$

$$\mathrm{c}_0 = \gamma\cos^2(\chi) + \sin^2(\chi), \tag{4.15}$$

$$P = \mathrm{M}g\frac{\rho_{\mathrm{helix}} - \rho_{\mathrm{liquid}}}{\rho_{\mathrm{helix}}}, \tag{4.16}$$

$$\Phi = \frac{2\pi}{\lambda}\frac{\cos\chi}{K_{\parallel}L(\mathrm{c}_0+\gamma)}P, \tag{4.17}$$

$$K = \frac{\gamma-1}{2\left(\frac{1}{4}\tan^2(\chi)\left((\gamma-1)\cos^2(\chi)+2\gamma\right) - \frac{(\gamma-1)^2\sin^4(\chi)}{8(\gamma+\mathrm{c}_0)} + \frac{1}{6}\left(\pi^2w^2\right)(\gamma+\mathrm{c}_0) - \mathrm{c}_0\right)}, \tag{4.18}$$

$$M = \frac{6(\gamma-1)\sin^2(\chi)}{\gamma\left(\frac{2}{\cos^2(\chi)}-7\right) - \frac{9((\gamma-1)^2\sin^4(\chi))}{2(\gamma+\mathrm{c}_0)} + \frac{2}{3}\pi^2w^2(\gamma+\mathrm{c}_0) + 5\mathrm{c}_0}, \tag{4.19}$$

in which L is the length of the helix, g the gravitational constant and $\rho_{\mathrm{helix}}, \rho_{\mathrm{liquid}}$ the mass density of the helix and the liquid, respectively. χ is the angle between the tangent to the helix and the z-axis of the helix, it describes the ratio between the radius and pitch of the helix. $1 \leq \mathrm{c}_0 \leq$ is a friction parameter which takes the aspect ratio of the helix into account. In the limit that $\chi \to 0$, the helix approaches a rod and $\mathrm{c}_0 \to 2$. If $\chi \to \pi/2$, the helix resembles a ring and $\mathrm{c}_0 \to 1$. P is related to the gravitational force and Φ is an inverse time scale parameter. M and K are dimensionless numbers describing the rate of rotation around the x- and y-axis, respectively, in the body frame independent of the orientation of the helix.

For simplicity the inverse time scale parameter is set to 1, $\Phi = 1$. Because the fluctuation in θ is very small, $\theta \approx \theta_0$, the initial angle. With that assumption the theory predicts the center of mass of the helix to perform a helical motion with radius R, frequency Ω and pitch length Λ around the z-axis in the lab frame:

$$R = \frac{3\lambda}{4\pi M}\left((c_0+\gamma)\frac{\gamma+1+(\gamma-1)\cos(2\chi)}{4\gamma} - 1\right)\sin(2\theta_0), \tag{4.20}$$

$$\Omega = \frac{2}{3}M\Phi \tag{4.21}$$

$$\Lambda = \frac{3\lambda}{2M}\left[2\cos^2\theta_0 + (c_0+\gamma)\frac{\gamma+1+(\gamma-1)\cos 2\chi}{2\gamma}\sin^2\theta_0\right], \tag{4.22}$$

with θ_0 defined as before. The helix will rotate very fast around its long axis with frequency

$$\omega_s = \frac{\Phi}{\gamma}(\gamma-1)(c_0+\gamma)\cos^2(\chi)\sin(\theta_0). \tag{4.23}$$

The long axis itself will keep its original angle and precess around with frequency $2/3M\Phi$. A schematic representation is shown in Fig. 4.5.

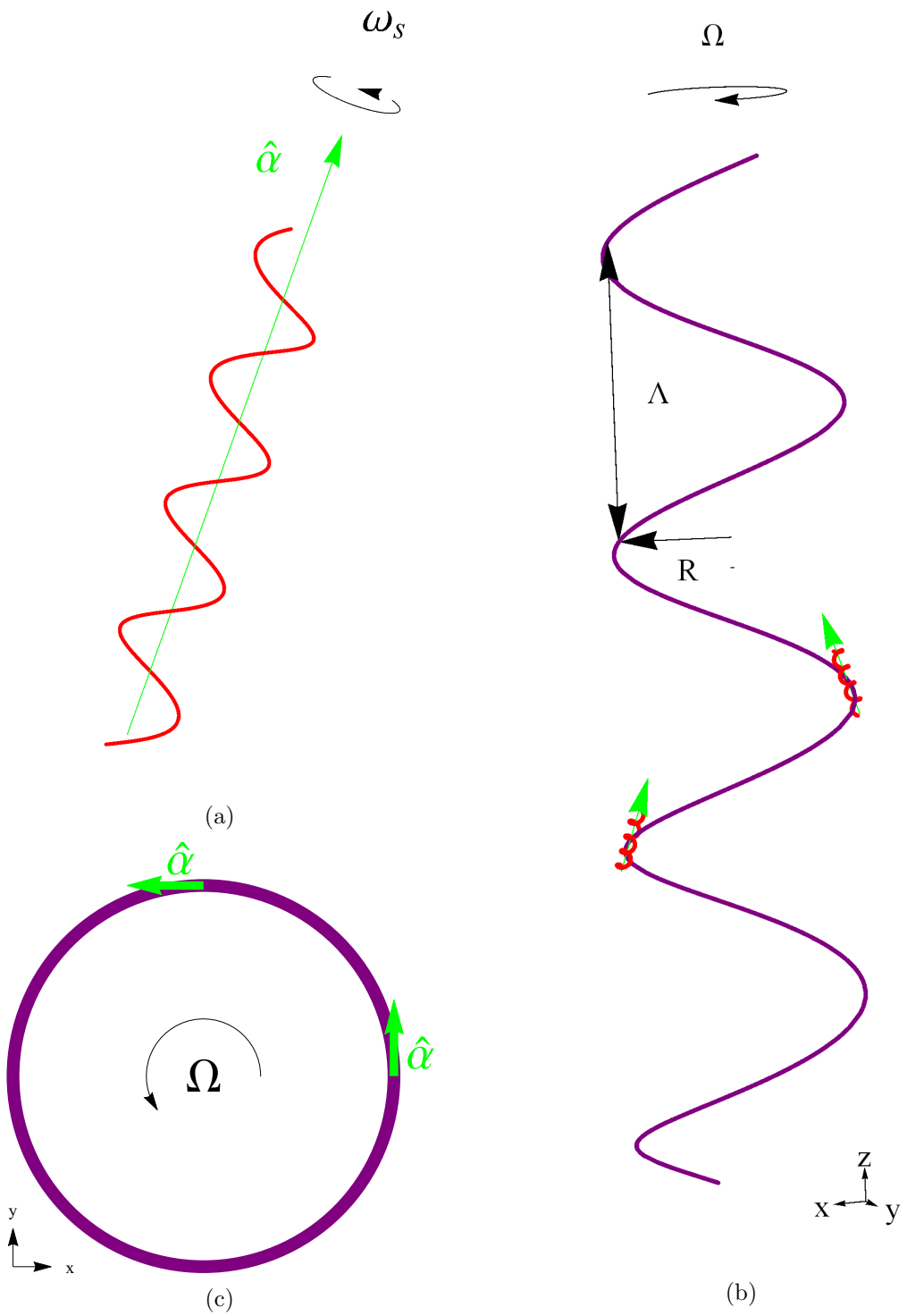

Figure 4.5: Schematic representation of the sedimentation behaviour of a helix. (a) The helix (red) rotates with frequency ω_s around its long axis $\hat{\boldsymbol{\alpha}}$ (green). (b) The sedimentation trajectory of the center of mass is shown in purple. The theory predicts the helix to sediment in a helical trajectory with radius R, pitch Λ and angular velocity Ω. For two different times, the helix and $\hat{\boldsymbol{\alpha}}$ are shown. The long axis $\hat{\boldsymbol{\alpha}}$ will precess, so that that the angle with the trajectory is constant. This can be seen clearly from above, shown in (c).

4.3 Sedimentation Trajectory Analysis

This section treats the parametrisation of the sedimentation behaviour of a helix, based on the theoretical prediction. Subsequently, the investigated helix parameters are presented. The approaches to quantify the influence of these parameters are explained. Finally, the characteristic units are introduced and the explored parameter space is discussed.

4.3.1 Analysis

Single helix

The theory predicts that the trajectory of the center of mass of the helix can be described as a helix with radius R, pitch Λ, and angular velocity Ω around the z-axis. The sign of Λ determines whether the helical trajectory is clockwise ($\Lambda > 0$), or anti-clockwise ($\Lambda < 0$). The different forms of rotation of the helix are shown in Fig. 4.6. The helix will rotate around its long axis with frequency ω_s, and $\hat{\boldsymbol{\alpha}}$ will precess around the z-axis with frequency $\omega_p = \Omega$. The theory assumes that $\theta = \theta_0$. We will investigate the deviation of θ from its original value θ_0. A small periodic fluctuation in θ, is called nutation. The frequency of this nutation is defined as ω_n, the amplitude of the deviation by $\Delta\theta$. The deviation of the center of mass from the pure helical trajectory, we describe as well by a radius R_d and angular frequency Ω_d.

We analyse how the above defined properties depend on:

- Bead separation δ: The distance between the beads influences the RPY matrix, as can be seen in Eq. 3.4. To investigate how slight changes in the distance affect the behaviour of the helix, we want to vary the relative distance δ/d. Therefore, we alter the number of beads per winding, while keeping all other parameters fixed at $r/d = 2, \lambda/d = 4\pi, \theta_0 = 0.3\pi, w = 3$.
- The ratio r/d, which we henceforward refer to as the 'inverse thickness' of the helix (note that in the theoretical model the thickness is in principle vanishing). The effect of the ratio between the radius of the helix and the diameter of the bead, r/d, is studied. The range of $1 \leq r/a \leq 10$ is examined, while keeping the ratio $\lambda/r = 1.5\pi$ fixed, for a helix with $w = 3$ and $\theta_0 = 0.3\pi$. We vary r/d by changing the bead diameter d and the number of beads N. This causes δ/d to vary between $1.205 - 1.38$.
- The starting orientation θ_0: The theory predicts that the behaviour depends on θ_0. We examine $\theta_0 \in [-0.5\pi, 0.5\pi]$. For all staring orientations, $\hat{\boldsymbol{\alpha}}$ and $\hat{\boldsymbol{\beta}}$ are initially in the yz-plane, $\hat{\boldsymbol{\alpha}} \times \hat{\boldsymbol{\beta}} = (1, 0, 0)$.
- The aspect ratio $w\lambda/2r$: the number of windings w, radius r and pitch λ, or the aspect ratio $w\lambda/2r$
- The chirality of the helix: $\lambda > 0$ for a right-handed helix, and $\lambda < 0$ for a left-handed helix.

The coordinates of the center of mass and the components of the spanning vectors $\hat{\boldsymbol{\alpha}}$ and $\hat{\boldsymbol{\beta}}$ are saved every 150 time steps as well as the angular and translational velocity of the center of mass. The simulations have run for $3 \cdot 10^6$ cycles, unless specified differently.

The following Mathematica 10 routines are used to determine the radii and angular frequencies. Two different approaches are used:

(i) FindPeaks is used to find the maxima and minima of the dataset, see Fig. 4.7a. The amplitude or radius R' of a (co)sine is 0.5(maximum − minimum). The period T' is the time between two maxima, which determines the angular frequency by $\Omega' = 2\pi/T'$. To compare the fit to the dataset, we also need to know the shift in position (dx) and frequency (ϕ'). The positional shift $dx = 0.5(\text{maximum} + \text{minimum})$. Finally, ϕ' can be found using the Mathematica routine FindFit applied to the function $R' \cos(\Omega' t + \phi') + dx$.

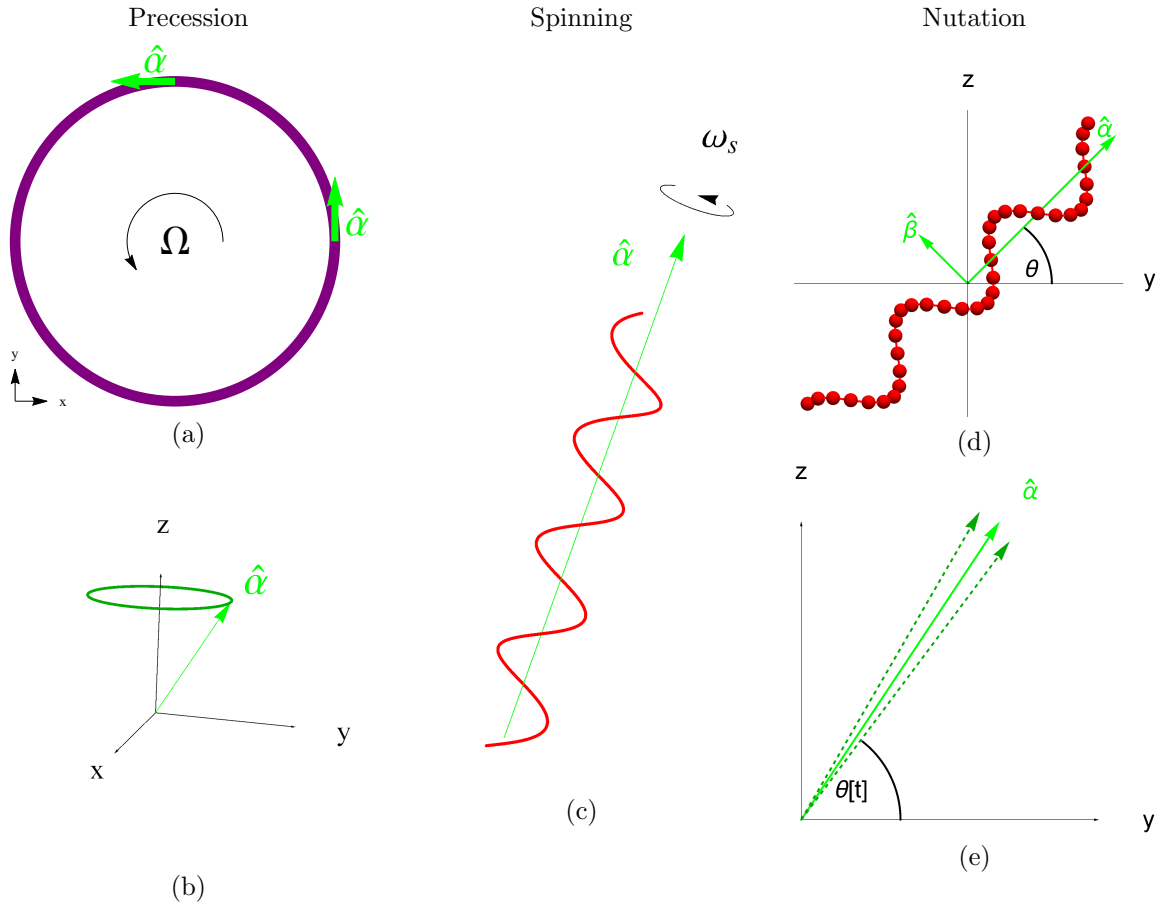

Figure 4.6: In (a), Ω is the angular velocity of the center of mass of the helix, the purple circle is the trajectory of the center of mass in the xy-plane. The x- and y-component of the long axis of the helix, $\hat{\boldsymbol{\alpha}}$ are predicted to change with the same frequency as the helical trajectory to keep the angle with the trajectory in the xy-plane fixed. This is called precession. The behaviour of $\hat{\boldsymbol{\alpha}}$ is clarified in (b). The spinning of the helix around its own long axis $\hat{\boldsymbol{\alpha}}$ with spinning frequency ω_s is displayed in (c). (d) The angle of the long axis with the xy-plane is defined as θ. (e) A periodic deviation of θ around an average value is called nutation. Here the average value is shown in light green, two deviating values in darker green.

(ii) NonlinearModelFit, see Fig. 4.7b, is used for the functions $R'\cos(\Omega' t+\phi')+dx$, $R'\sin(\Omega' t+\phi')+dy$ with ϕ' the phase shift, and dx, dy the shift in x and y, respectively. Initial guesses for the different parameters are made by eye, in order to ensure convergence of the algorithm.

The resulting function is plotted, to determine whether it resembles the data points. The choice which of the methods is used, is based on which method is applicable and leads to the correct results.
All the methods are applied on either the x-coordinate as a function of time, or the y-coordinate as a function of time. Except when we indicate otherwise.

R_d and Ω_d are determined by applying method (i) on the first 200 data points regarding the x-coordinates of the center of mass. For the helical trajectory, method (i) is used on the x-coordinates, if the number of windings regarding the trajectory is larger than 4. The data set is adapted to account for the periodic deviation: only the data points separated by n time steps are taken into consideration, where n is based on Ω_d. The values are checked by applying method (ii). For smaller winding numbers only method (ii) is applied. Because for most parameters $R_d/R \ll 0.05$, the error in method (ii) due to the periodic deviation can be neglected.

To determine ω_s, method (i) is applied to the dataset of the x-coordinate of the short axis $\hat{\boldsymbol{\beta}}_x$. To find the frequency of the precession ω_p, first all the maxima and minima of $\hat{\boldsymbol{\alpha}}_x$ are determined, see Fig.

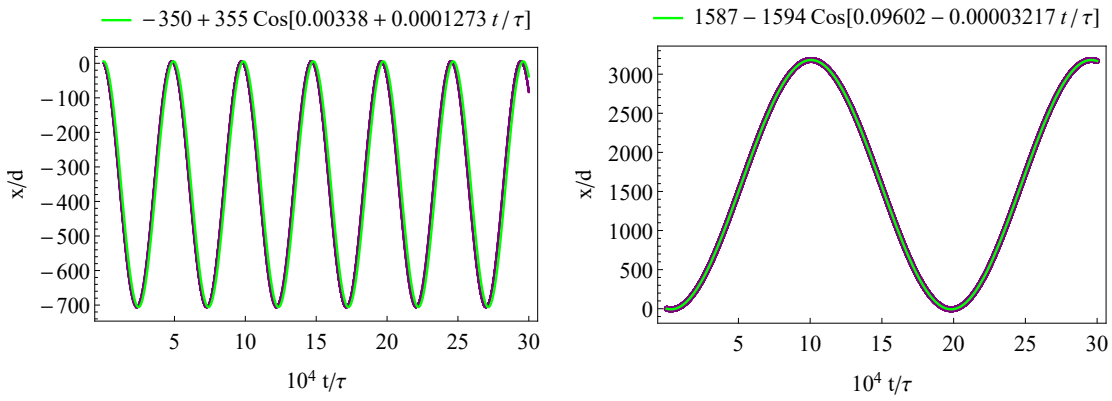

(a) Method (i)

(b) Method (ii)

Figure 4.7: Example of the fitting methods. The figures show the x-coordinate x/d of the center of mass of a helix as a function of time t/τ. The simulation data is shown in purple, the fitted function in green. (a) Method (i) is applied to a helix with parameter settings $N = 37$, $w = 3$, $r/d = 1.5$, $\lambda/d = 4\pi$, $\theta_0 = 0.25\pi$. (b) Method (ii) is applied to a helix with settings $N = 52$, $w = 3$, $r/d = 2$, $\lambda/d = 4\pi$, $\theta_0 = 0.3\pi$. The fits correspond well with the datapoints. A small error can be seen in the value for ϕ for method (i).

4.8 for an example. The spinning frequency is much higher than the precession frequency, consequently those peaks are completely determined by the spinning frequency. The sine corresponding to the precession determines the mean of $\hat{\boldsymbol{\alpha}}_x$ as a function of time. Therefore every maximum is averaged with its left neighbouring minimum, to generate the mean as a function of time. Accordingly method (ii) is applied on this new dataset to find ω_p.

The nutation frequency ω_n is acquired by applying method (i) to the dataset of $\hat{\boldsymbol{\alpha}}_z$. The mean of $\hat{\boldsymbol{\alpha}}_z$ is calculated, to find the angle around which $\hat{\boldsymbol{\alpha}}$ nutates by $\theta = \arcsin \hat{\boldsymbol{\alpha}}_z$. We use the same equation on the maximum and minimum of $\hat{\boldsymbol{\alpha}}_z$ for the amplitude of the deviation $\delta\theta$.

The velocity v_z is used to calculate the pitch length $\Lambda = v_z T = v_z 2\pi/\Omega$. v_z is found by fitting a linear function $a + bt$ to the z-coordinate as function of time, in which $b = v_z$, see Fig. 4.9 for an example. The Mathematica 10 routine FindFit is used for this procedure.

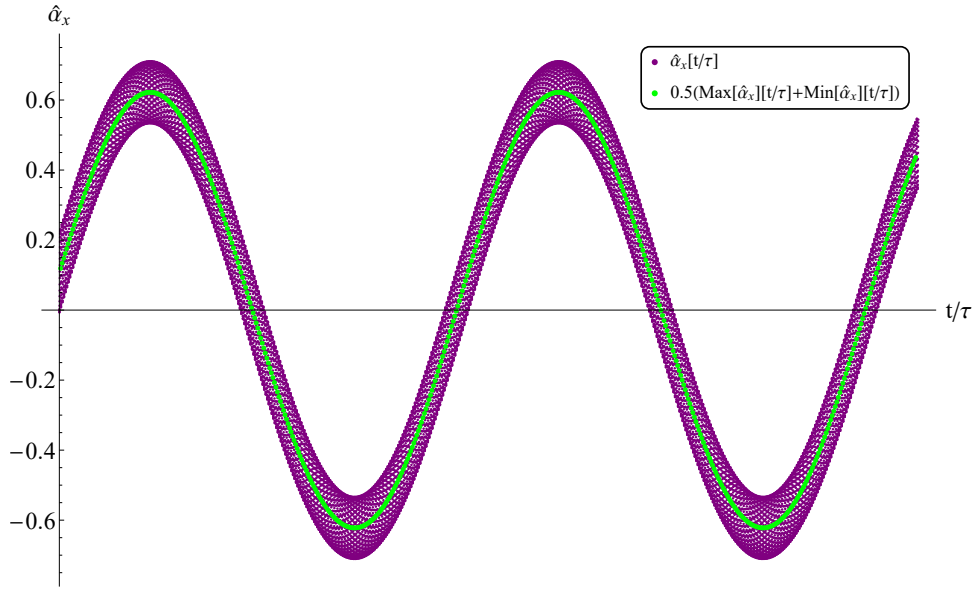

Figure 4.8: Example of a dataset of $\hat{\boldsymbol{\alpha}}_x$ and its mean as function of time. The x-coordinate of the long axis of the helix $\hat{\boldsymbol{\alpha}}$ is displayed as function of time. The purple points display all the datapoints. The mean of a maximum and the next minimum as a function of time are displayed in green. The mean values are used to calculate the precession frequency.

Two helices

We briefly studied the sedimentation behaviour of two helices. We qualitatively investigated their trajectory as a function of the initial distance between the two helices, Δ_0. We wanted to examine the effect of the orientation of the helices, in a controlled manner. Therefore the initial angle θ_0 is equal for both helices and the two extremal values are considered: $\theta_0 = 0$ for horizontally aligned helices, and $\theta_0 = \pi/2$ for vertically aligned helices. An example of two horizontally aligned helices is shown in Fig. 4.10a. For the vertically oriented helices, we also investigated how the trajectory depends on the chirality q of the helices.

Let the centre of helix 1, $\mathbf{R}^1_{\mathrm{CM}}$, be positioned in the origin. For $\theta_0 = 0$, the centre of helix 2 is placed at $\mathbf{R}^2_{\mathrm{CM}} = \Delta_0\hat{x}$, with $\Delta_0/d = 6, 8, 10$, with d the bead diameter. The chiralities of the helices, q_1, q_2, are equal: $q_1 = q_2 = 1$. For $\theta_0 = \pi/2$, the centre of helix 2 is placed at $\mathbf{R}^2_{\mathrm{CM}} = \Delta_0\hat{y}$, with $\Delta_0/d = 5, 6, 8, 10$ and $q_1 = q_2 = 1$. Then, for $\Delta_0/d = 6$, we investigated the possible chirality configurations: $q_1 = \pm q_2$, $q_2 = \pm 1$, see Fig. 4.10b.

To analyse the behaviour of the two helices, we qualitatively investigate the trajectory of the center of mass of the system of two helices $\mathbf{R}_{\mathrm{CM}} = 0.5(\mathbf{R}^1_{\mathrm{CM}} + \mathbf{R}^2_{\mathrm{CM}})$. We study the distance between the two helices $\Delta/2d$ as a function of time as well as the relative distance in z between the two helices. The orientation of $\hat{\boldsymbol{\alpha}}$ for both helices and the relative phase shift in $\hat{\boldsymbol{\beta}}$, $\delta\phi$, are also considered. Method (ii) of fitting is applied to the dataset of $\hat{\boldsymbol{\beta}}_x$ for both helices. The relative phase shift is $\delta\phi = |\phi_1 - \phi_2|$.

4.4 Parameter settings

In the simulations the characteristic units are such that the bead diameter $d = 1$, the gravitational force applied to the center of mass of the helix $\mathbf{F}_{\mathrm{CM}} = -40\hat{z}$ and the viscosity $\eta = 1$. This means that the distance is measured in units of d, force in units of $f_0 = 1/|\mathbf{F}_{\mathrm{CM}}$, torque in units of $f_0 d$, velocity in $f_0/\eta d$,

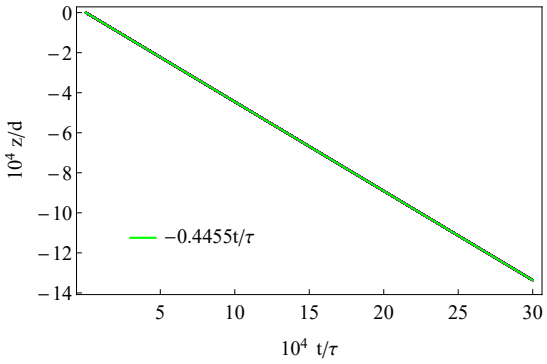

Figure 4.9: Example of a dataset and fit to find v_z. The z-coordinate of the center of mass is plotted as a function of time t/τ. The data is shown in purple, the fitted function $z(t/\tau) = -0.4455t/\tau$ in green. As can be seen, the fitted function describes the data well.

angular velocity in $f_0/\eta d^2$ and time in $\tau = \eta d^2/f_0$.

The choices for the investigated parameters are listed below:

- The gravitational force is set to $40 f_0 = \mathbf{F}_{\mathrm{CM}}$. Because a gravitational force on a rigid body induces no torque, we can set the torque on the center of mass to zero.
- The bead separation δ/d is altered between 1.1 and 2. The RPY-method breaks down at small bead separations, because it does not include the lubrication forces. On the other hand, the bead model needs to resemble a solid body, so the distances cannot be too large.
- The range of $2 \leq r/a \leq 20$ is examined, while keeping the ratio $\lambda/r = 1.5\pi$ fixed.
- We chose parameters such that $0 \ll \chi \ll \pi/2$, in order for the helix not to be too rod- or ring-like, namely: r/d is varied between 1 and 3 and λ/d between 1.2π and 8π.
- The number of windings w is varied between 1 and 7. The computation time increases as a power of the number of beads. Every winding is composed of at least 9 beads. The expectation is that when the number of windings is sufficiently large, adding a winding will not have a large impact. Therefore a balance between computation time and exemplary helical behaviour has to be found. We have chosen to run most simulations for $w = 3$, to reduce the overall computation time and allow for exploration of the maximal amount of parameter space.
- The range of the starting orientation θ_0 is $[-0.5\pi, 1.35\pi]$.

For a helix with parameter settings $r = 3, \lambda = 3, w = 4$ the results are compared to Lattice-Boltzmann simulations done by Dr. J. de Graaf, using the ESPResSo software package [32]. The helix is build up out of 200 beads, which have a diameter $\sigma \approx 1.2$ lattice spacing. In the LB simulation the gravitational force $\mathbf{F}_{\mathrm{CM}} = -0.1\hat{z}$, the viscosity $\eta = 1$ and the time step $\mathrm{d}t = 0.01$. The starting angles investigated are $\theta_0 = 1.15\pi, 1.25\pi, 1.35\pi$. The time for the results of the LB simulations is scaled to allow for comparison. The time is measured in units of $\tau = \eta d^2/f_0$: A factor of $1/40$ is obtained by the difference in gravitational force, another factor of $1/1.2^2$ by the difference in bead diameter. Thus, the resulting time scaling factor is $1/40 \times 1/1.2^2 = 1/57.6$. For the RPY method distances are measured in units of the bead diameter, while for the LB method distances are measured in lattice spacings. To equalise the units, the results for the LB simulations are scaled with a factor of $1/1.2$, since the bead diameter of the LB method was approximately 1.2.

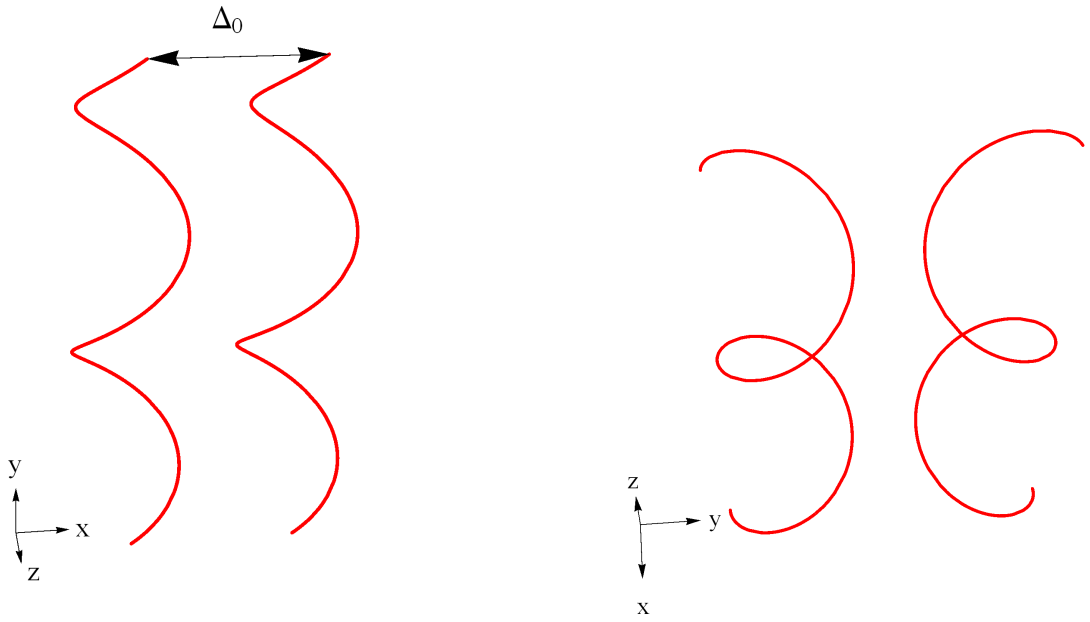

(a) (b)

Figure 4.10: Schematic representation of the orientation of two helices. (a) Two horizontally aligned helices. The distance between the two helices is Δ_0 is directed along the x-axis. The helices are parallel along the y-axis. They have the same chirality $q = 1$. (b) Two vertically aligned helices with opposite chirality. The left helix has chirality $q_1 = 1$, the right helix $q_2 = -1$.

Chapter 5

Verification

This chapter discusses the simulation results of the simple bodies (sphere, dumbbell, L-shape) used to verify our model. The first section treats the sedimentation of a single bead sphere, which we studied to test the basic implementation. The implementation of the RPY method for multiple spheres is tested in the next section. The results are compared to results obtained by Stokesian dynamics. Then, in the third section, the coefficients of the mobility matrix of a dumbbell are investigated. Finally, the model is tested for an L-shaped particle.

5.1 Single bead

The sedimentation of a single bead is investigated. A bead can be described by the position of its center $\mathbf{R}_{\mathrm{CM}}$ and its radius a. When it sediments in a fluid, it should move in a straight line without accelerating. The velocity should only have a z-component, $\mathbf{v} = 0, 0, v_z$, with $v_z = F_z/(6\pi\eta a)$ according to Stokes-Einstein theory [2], with η the viscosity and where we assume that the sign is absorbed in the gravitational force F_z, see Chapter 3. We test this for a sphere with bead radius $a = 1$, and gravitational force $F_z = -40\eta d^2/\tau$, with d the bead diameter and τ our time-scale parameter. We found that the velocity of the bead indeed only had a z-component. The value of $v_z\tau/d$ was found by dividing the difference between the final z-coordinate, z_f, and the initial z-component, z_0, by the time past t/τ: $v_z\tau/d = (z_f/d - z_0/d)/t\tau = -4.24412$. We compare this to the theoretical expression $v_z\tau/d = F_z/(6\pi\eta a)\tau/d$ which is $F_z/(6\pi\eta a)\tau/d = -40/3\pi = -4.24413$. The theoretical value and the simulation value are in agreement up to order 10^{-4}. Therefore, we conclude that the method is correctly implemented for one sedimenting bead.

5.2 Two beads

To test whether the RPY matrix was implemented correctly, we simulated two sedimenting spheres and compared the results to Stokesian Dynamics (SD) simulations. The SD simulations were made using the Mathematica notebooks developed by Dr. H. Binous [33], based on Fortran 77 codes made by Prof. R. J. Philips and Dr. H. Binous [33]. For the RPY method, we used two modelling methods. We modelled the spheres as independent spheres and as two rigid bodies, see Chapter 3 for an explanation of the methods. The first RPY modelling method is used to verify whether the RPY method leads to the correct physical results by comparing to the SD simulation results. The second RPY modelling method is used to verify that the procedure for calculating the RPY-matrix for multiple rigid bodies is implemented correctly. If this is implemented correctly, the results should be the same.

We set the radius of the beads to be $a = 1$. Bead 1 is placed in the origin, bead 2 at $(0, \Delta_0 \cos\theta, \Delta_0 \sin\theta)$, with Δ_0 the initial distance between the beads and θ the angle between the line connecting the centres of the beads and the y-axis. For $\Delta_0/a = 4$, $\theta = \pi/6$, the comparison between the results for the trajectory of two sedimenting spheres obtained by the RPY method and the SD method is shown in Fig. 5.1a. The behaviour is similar for both methods: the beads sediment diagonally in the direction of the bead which has the smallest z-component. However the angle between the trajectory of the beads and the z-axis, ϕ,

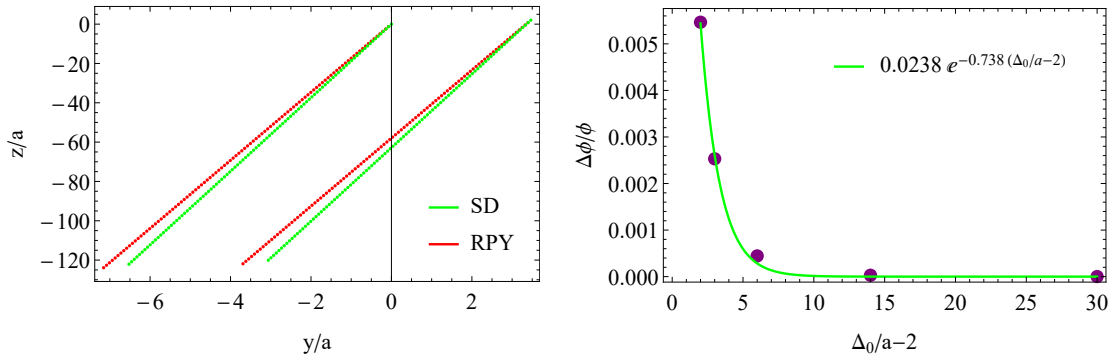

(a) (b)

Figure 5.1: Comparison between the results obtained with the RPY method and the SD method for the sedimentation of two spheres. (a) The yz-trajectory of the two spheres at an initial distance $\Delta_0/a = 4$, and angle $\theta = \pi/6$ is shown. The trajectories for the RPY method are displayed in red, the SD method in green. The beads move diagonally. (b) The relative angle between the trajectories obtained by the RPY and the SD method, $\Delta\phi/\phi$, is plotted as a function of the distance between the two spheres, Δ_0/a. The difference $\Delta\phi/\phi$ between the two trajectories exponentially decays with the distance. In far-field both methods agree.

is smaller for the SD method, than for the RPY method. We have plotted the relative difference in the trajectory angle, $\Delta\phi/\phi$, as a function of the initial distance Δ_0/d, see Fig. 5.1b. The difference is small for $\Delta_0/a = 4$, namely $\Delta\phi/\phi = 0.005$, and decreases exponentially with Δ_0/a. Thus, in the far-field the results for both methods are the same, in the near-field there is a small deviation. This is precisely what we expected, because the RPY method does not take into account lubrication forces, which play a role when the beads are in close proximity to one another.

To test whether we had implemented the procedure to calculate the RPY matrix for multiple rigid bodies correctly, we did the simulations for the same parameter settings, now including the coupling as described in Chapter 3. The results agreed up to numerical precision. Thus, we can conclude that the matrix to calculate the hydrodynamic interactions between multiple rigid bodies is implemented correctly.

5.3 Dumbbell

In the previous section, we have seen that at small distances, where lubrication forces start to play a role, the error in the results for the RPY method increases. To test how this error affects the behaviour of a rigid body, we study the coefficients of the mobility matrix for a dumbbell shaped particle. These coefficients describe the couplings between translations and rotations. The coefficients of the mobility matrix of a dumbbell are compared to the values obtained by Fischer *et al.* [18]. In our simulations the two spheres have the same radius a, the distance r between the centres is set such that the beads are touching $r = 2.006a$. The results are shown in Table 5.1.

The translational-translational and the rotational-rotational mobility matrices are indicated with μ^{tt} and μ^{rr} respectively. The components of the mobility matrix parallel to the long axis of the dumbbell is denoted by $\parallel$ and the component perpendicular to the long axis by $\perp$.

The cross-coupling terms of the mobility matrix are all zero or $< 10^{-16}$, thus within numerical accuracy equal to zero, which is what we expected. The values for $\mu^{tt}_{\perp}, \mu^{rr}_{\parallel}$ and $\mu^{rr}_{\perp}$ agree within the error. For the RPY method $\mu^{tt}_{\parallel}$ is higher than the values obtained by the other methods. The error is 5% of the literature value. A disagreement between the components is in line with our expectations, as we have already seen that for two spheres, a slight difference in sedimentation angle could be observed. However, it is remarkable that the other components are in good agreement. We conclude that the agreement is good enough to trust the validity of the results obtained by the RPY method.

Method	$\mu_{\parallel}^{tt}/\mu_0^{tt}$	$\mu_{\perp}^{tt}/\mu_0^{tt}$	$\mu_{\parallel}^{rr}/\mu_0^{rr}$	$\mu_{\perp}^{rr}/\mu_0^{rr}$
Raspberry, filled[18]	0.77 ± 0.01	0.69 ± 0.01	0.55 ± 0.01	0.27 ± 0.01
HYDRO++[27]	0.77 ± 0.01	0.70 ± 0.01	0.55 ± 0.01	0.27 ± 0.01
RPY	0.81	0.70	0.56	0.27

Table 5.1: Comparison between the coefficients of the mobility matrix of a dumbbell obtained by the RPY method, the Raspberry model [18] and HYDRO++ model [27]. μ^{tt} and μ^{rr} are the translational-translational and rotational-rotational mobility matrices. $\perp$ and $\parallel$ denote that the component of the mobility matrix is perpendicular or parallel, respectively, to the long axis of the dumbbell. The results are non-dimensionalised by dividing the components by their corresponding terms for a sphere with the same radius as one of the lobes, μ_0. The values for $\mu_{\perp}^{tt}, \mu_{\parallel}^{rr}$ and $\mu_{\perp}^{rr}$ agree within the error. For the RPY method $\mu_{\parallel}^{tt}$ is slightly higher than the values obtained by the other methods.

5.4 L-shaped particle

As a final test we study the final angle under which an L-shaped particle sediments. The starting angle θ_0 is varied between 0 and $\pi/2$. The L-shape was modelled for four beads and for 32 beads, as described in subsection 4.1.2. The results are compared to the value experimentally obtained by Hagen *et al.* [28]. The results can be found in Table 5.2. The terminal angle θ_f under which the L-shape sediments is the same for every starting angle θ_0 varying between 0 and $\pi/2$, but depends slightly on the number of particles. The final angle under which the L-shape sediments is 0.6° higher than the experimental value

Method	Angle θ_f
RPY NB=4	56.6°
RPY NB=32	54.6°
Experimental by [28]	56°

Table 5.2: Comparison of the terminal angle θ_f of a sedimenting L-shaped particle between simulation results and experimental results. For the RPY method the L-Shape was modelled using NB beads, with $NB = 4, 32$. The experimental value was obtained by [28].

of [28] for $NB = 4$ and 1.4° lower for $NB = 32$. A possible explanation for the differences could be the roughness of the modelled shape, which influences the flow around the particle. Since the deviation in the terminal angle is small, we conclude that the RPY method for rigid bodies built up out of beads leads to satisfying physical results.

Chapter 6

Results

In this chapter we treat the results for the sedimentation of one and two helices. The results for a single helix are introduced and discussed in the first section. To verify the results, they are also compared to theory and results obtained from lattice-Boltzmann simulations. The second section introduces several results for the sedimentation of two helices.

6.1 Single Helix

This section treats the sedimentation of a single helix. In the first subsection we investigate the influence of the distance between the beads, by which we approximate the helix, on the results. In the following subsections we study the influence of the thickness, starting orientation, chirality, and aspect ratio on the sedimentation behaviour. Finally, to verify the results, we compare these to the theoretical expressions derived by Dr. A. Morozov and lattice-Boltzmann simulation results performed by Dr. J. de Graaf.

6.1.1 Distance between beads

Here, the distance, δ, between the beads by which we approximate the helix is studied. Specifically, we investigate the change in the helix' trajectory, which itself is helical. To tune δ, we have varied the number of beads N between 37 and 52 for a helix with parameter settings $r = 2, \lambda = 4\pi, w = 3, \theta_0 = 0.3\pi$. Figure 6.1b shows the radius of the helical movement, R, and the pitch length, Λ, as a function of the bead distance δ/d, with d the bead diameter. R and Λ increase with increasing bead distance. The data show convergence of the result for both parameters when $\delta/d \to 1$, although the helix is still not smooth.

In Fig. 6.1c the deviation of the angle θ from its original value is shown as a function of the bead distance. θ is the angle that the long axis $\hat{\boldsymbol{\alpha}}$ of the helix makes with the xy-plane. We have plotted the average orientation angle, $\langle\theta\rangle_t$, and the maximum and minimum orientation angle, $\mathrm{Max}[\theta], \mathrm{Min}[\theta]$. These values are constant for $\delta/d < 1.38$. The difference between the extrema and the average angle is the nutation amplitude. A schematic picture is shown in Fig. **??**, where the long axis is displayed for three different angles θ. The amplitude and average of θ do not change for $\delta/d < 1.38$, thus the nutation is not influenced by differences in bead distance, which indicates that the nutation is not caused by the irregularities of the helix.

Note, that these data are obtained for specific parameter settings for the helix, it is possible that the results differ for other settings, but as long as the separation is kept small, $\delta/d \approx 1$, this should not be an issue. The RPY-method is actually a far-field approximation. This means that while the result converges for small bead separations, the quality of the RPY approximation breaks down. However, the comparison of the results for the dumbbell and the L-shape in Chapter 5 showed good agreement for a bead distance $\approx 1.005d$. In the light of the above, a bead distance of $1.01 \leq \delta/d \leq 1.1$ is preferable.

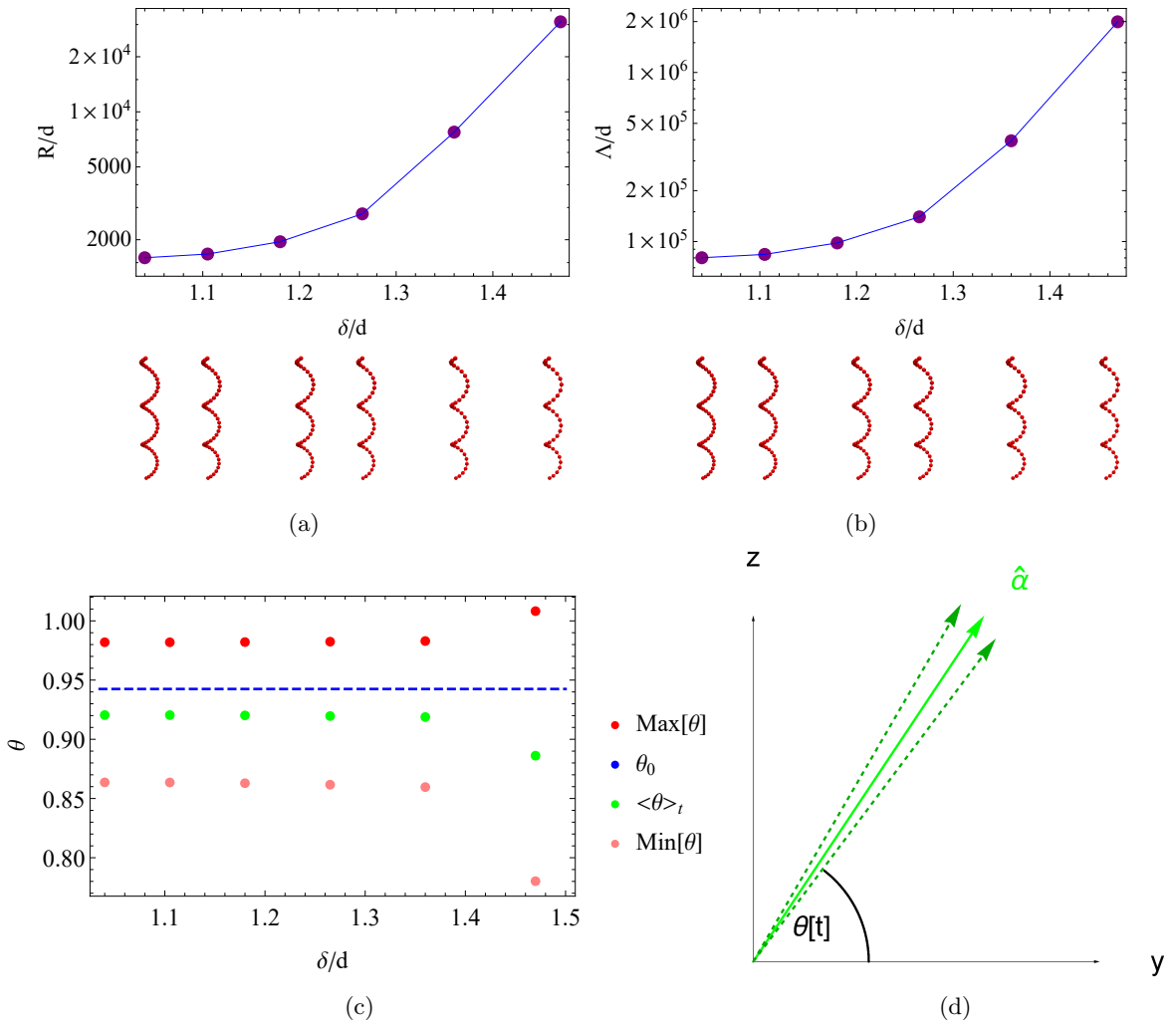

Figure 6.1: Change of the trajectory as a function of the relative distance between the beads. The bead distance δ/d is modified by varying the number of beads N between $37-52$ while the other parameters determining the helix are kept constant. (a) The trajectory radius R and (b) the trajectory pitch Λ are displayed as a function of the bead distance δ/d. Convergence is observed for both parameters when $\delta/d \to 1$. Visualisations of the helix are displayed below the horizontal axis for the corresponding bead distances. (c) The average orientation angle, $\langle\theta\rangle_t$, and the maximum and minimum orientation angle, $\mathrm{Max}[\theta], \mathrm{Min}[\theta]$ are plotted as function of δ/d. These measure the orientation of the helix' long axis w.r.t. the xy-plane. For comparison also the starting orientation θ_0 is displayed. The values are constant for $\delta/d < 1.38$, for $\delta/d = 1.38$, $\langle\theta\rangle_t$ decreases, and the nutation amplitude, the difference between the extrema and the average angle, increases. (d) A schematic picture of the long axis of the helix $\hat{\boldsymbol{\alpha}}$ for different values of θ. The helix has parameter settings $r = 2, \lambda = 4\pi, w = 3, \theta_0 = 0.3\pi$.

6.1.2 Thickness

The thickness of the helix, described by the inverse thickness parameter r/d, is studied, by considering the change in helical trajectory and nutation. The range of $1 \leq r/d \leq 10$ is examined, while keeping the ratio $\lambda/r = 1.5\pi$ fixed for a helix with $w = 3$ and $\theta_0 = 0.3\pi$. We vary r/d by changing the bead diameter d and the number of beads N, whereas r is kept fixed.

The results for the behaviour of the center of mass, as well as the effect on the nutation are shown in Fig. 6.2. Three different regimes can be distinguished from the results for the trajectory radius R and pitch Λ. For very thick helices, $r/d < 1.45$, there is no helical trajectory: $R = \Lambda = 0$. The helix orients itself with the long axis $\hat{\boldsymbol{\alpha}}$ in the xy-plane and drops straight down. Then for $1.45 < r/d \leq 2.15$, R and

Λ strongly increase with r/d. The handedness of the helical trajectory is equal to the handedness of the helix. For $r/d = 2.5$ the trend is broken and the handedness of the helical trajectory has changed sign. For $r/d > 2.5$, R and Λ slightly decrease as a function of r/d. However, the error in the analysis is larger for the thin helices, because less of the trajectory was completed. Thus, more and longer measurements are needed to determine the trend for thin helices.

To check that differences in bead distance did not influence the observed behaviour, we have run two simulations with different N for some values of r/d. Although the difference in δ/d leads to quantitative changes, the overall trend (i.e., the qualitative result) is the same.

These results indicate that the sedimentation behaviour is strongly dependent on the thickness of the helix. We suspect this to be a physical property of the system, and not a flaw in our model. When the thickness decreases the friction of the helix will reduce significantly. The ratio between the perpendicular and parallel friction coefficients is much smaller for thick helices then for thin helices.

In Fig. 6.2c, the change in the angle θ — which measures the orientation of the helix' long axis w.r.t. the xy-plane — from its original value is shown as a function of r/d. The maximum, minimum and average value of θ are presented, just as the initial angle. The average orientation angle, $\langle\theta\rangle_t$, is lower than the starting orientation, θ_0, and the difference is larger if the helix is thicker. However, if we ignore the thickest regime, where the helices just sediment down, $\langle\theta\rangle_t$ follows a smooth curve. The difference in nutation could be caused by the roughness of the helix. But we have seen in Subsection 6.1.1 that the nutation does not change if the bead distance δ/d is sufficiently small: $\delta/d < 1.38$. Therefore, we think it is more likely that the nutation is caused by the physics of the system. The friction with the fluid is stronger for thick helices.

Although the thin helices are less dependent on the precise values of r/d and the theoretical approach was based on infinitely thin helices, they also require more beads. Since the computation time scales with $N^{2.5}$, the number of beads we can use is limited. Therefore, we decide to examine mainly the regime of thick helices, $r/d \leq 2$.

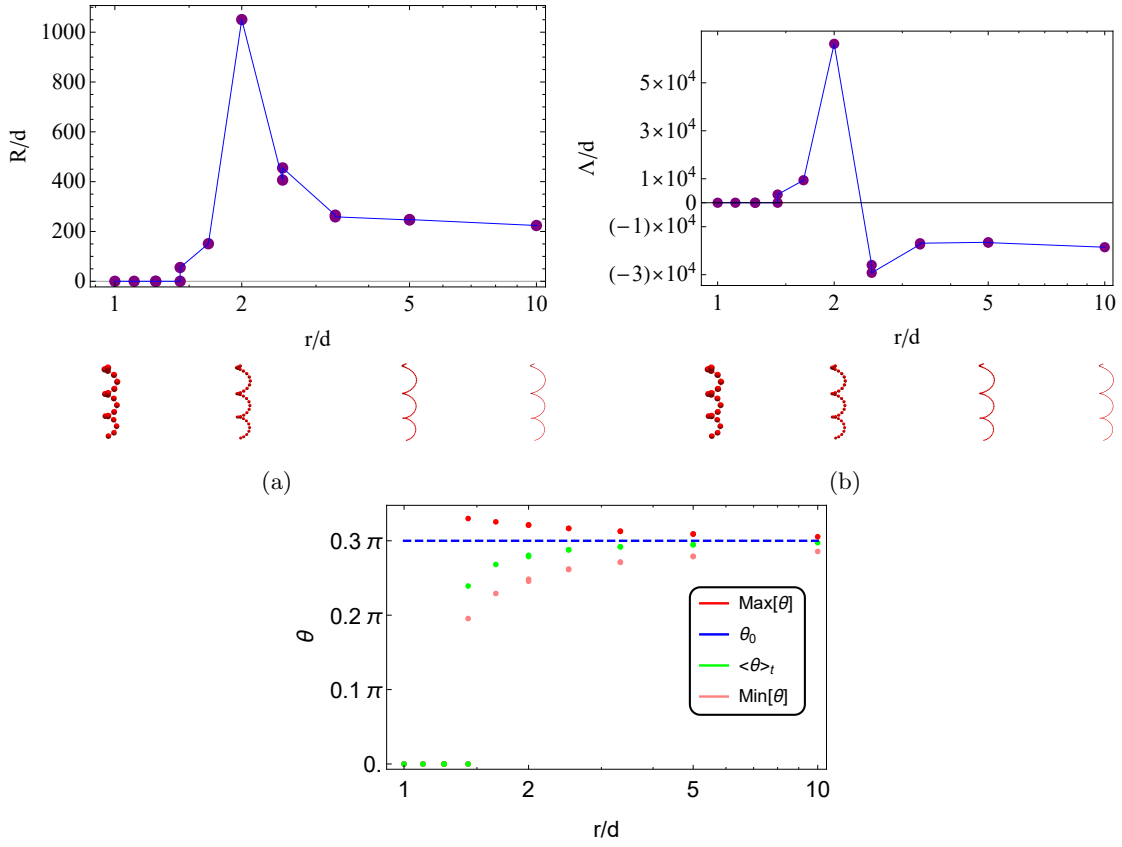

(a) (b)

(c)

Figure 6.2: The sedimentation behaviour as function of the thickness of the helix. The thickness r/d is varied while keeping the other parameters fixed; $\lambda/r = 3/2\pi, w = 3, \theta_0 = 0.25\pi$. (a) The radius of the trajectory R and (b) its pitch Λ are shown as function of r/d. The horizontal axis has a logarithmic scale, to visualise that their behaviour can be divided into three regimes. Below the horizontal axis the helices with corresponding thickness are shown. For $r/d < 1.45$, $R = 0, \Lambda = 0$, which means that the helix drops straight down. Then both parameters steeply increase for $1.45 < r/d \leq 2.15$ until $r/d \approx 2.15$. Finally, for $r/d \geq 2.55$, their values gradually decrease. (c) The fluctuation of the angle θ is shown as function of r/d. The starting angle θ_0 is shown in blue, the time-average of the angle, $\langle\theta\rangle_t$ in green, the maximum angle in the simulation, Max$[\theta]$, in red and the minimum, Min$[\theta]$, in pink. The deviation from the starting angle θ_0 is higher for lower values of r/d, thus for thicker helices. The values for $r/d < 1.45$ are obtained after their initialisation period, so when the helices have started falling straight down.

6.1.3 Starting Orientation

We investigate the influence of the starting orientation on the behaviour of the helix. For a number of positive and negative values of θ_0 we compare the radius R and the pitch Λ of the helical movement. The parameter settings used in this subsection are $r/d = 2$, $\lambda/d = 3\pi$, $w = 3$, $N = 37$.

The difference for positive and negative values in θ_0 is shown in Table 6.1. The radius R, the pitch Λ and the handedness of the helical trajectory are equal. The center of the helical trajectory MP is mirrored in the xy-plane. The trajectories for $\theta_0 = \pm 0.3\pi$ are visualised in Fig. 6.3. It can be seen that the behaviour is the same, but that the starting point in the trajectory is shifted over half a period. This causes the centres $MP_\pm$ to be mirrored in the xy-plane, and is simply an effect of the geometry of the helix. For opposing signs in the starting orientation, $\hat{\boldsymbol{\alpha}}$ is mirrored in the y-axis, and $\hat{\boldsymbol{\beta}}$ is mirrored in the z-axis, which results in a helix which is rotated 180° degrees in the xy-plane, as is visualised in Fig. 6.4. Since the direction of gravity is along $\hat{z}$, we study the same physical, but rotated, system.

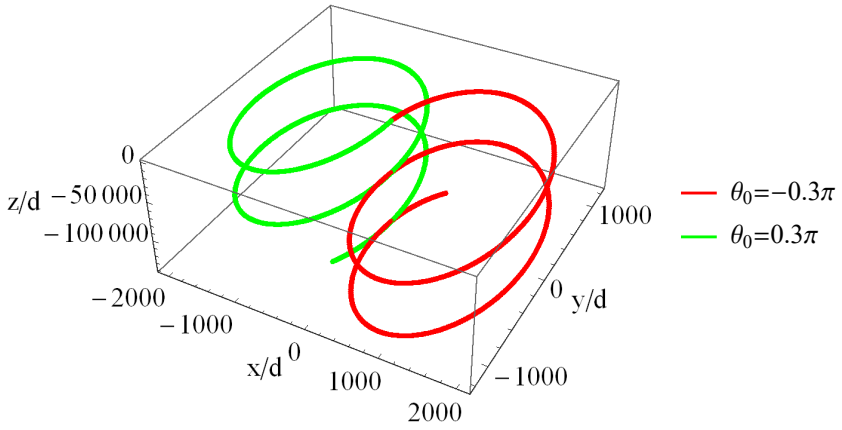

Figure 6.3: Comparison between the two trajectories of single sedimenting helix. The red trajectory is for $\theta_0 = -0.3\pi$, $\theta_0 = 0.3\pi$ is displayed in green. The starting point of the trajectory is rotated over 180°.

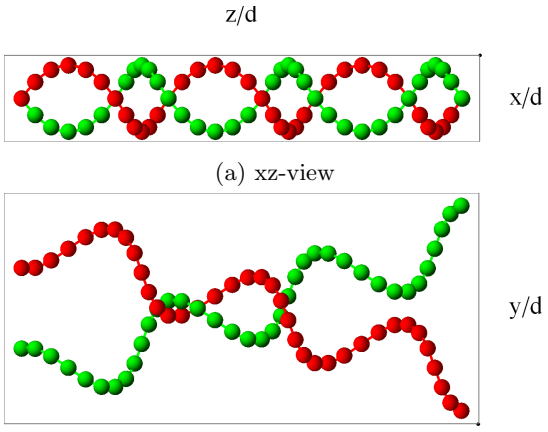

(a) xz-view

(b) yz-view

Figure 6.4: The orientation of a single helix with opposing signs for the starting orientation. For $\theta_0 = 0.4\pi$ the helix is shown in red, the green helix has $\theta_0 = -0.4\pi$. The helix is rotated 180° degrees around $\hat{z}$ for the different starting orientations.

The starting orientation is varied between a horizontally oriented helix ($\theta_0 = 0$) and vertical helix

$\lvert\theta_0\rvert$	R_+/d	R_-/d	Λ_+/d	Λ_-/d	MP_+/d	MP_-/d
0.1π	0	0	-	-	$(1.14899, -6.25893)$	$(-1.14899, 6.25893)$
0.25π	355.46	355.46	491.45	491.45	$(-350.1, 55.76)$	$(350.1, -55.76)$
0.3π	1050.58	1050.58	1365.81	1365.81	$(-1034.2, 181.60)$	$(1034.2, -181.60)$
0.4π	∞	∞	∞	∞	$(-0.14144, -0.43861)t/\tau$	$(0.14144, 0.43861)t/\tau$
0.5π	1113	1113	6323	6323	$(0, -1114.5)$	$(0, 1114.5)$

Table 6.1: The trajectory parameters for different starting orientations. Values for positive (+) and negative (−) θ_0 are compared. MP denotes the center of the helical trajectory in the xy-plane. The radius R and the pitch Λ of the helical trajectory do not depend on the sign of θ_0, but MP does. The center of the trajectory is rotated 180° in the xy-plane for opposing signs.

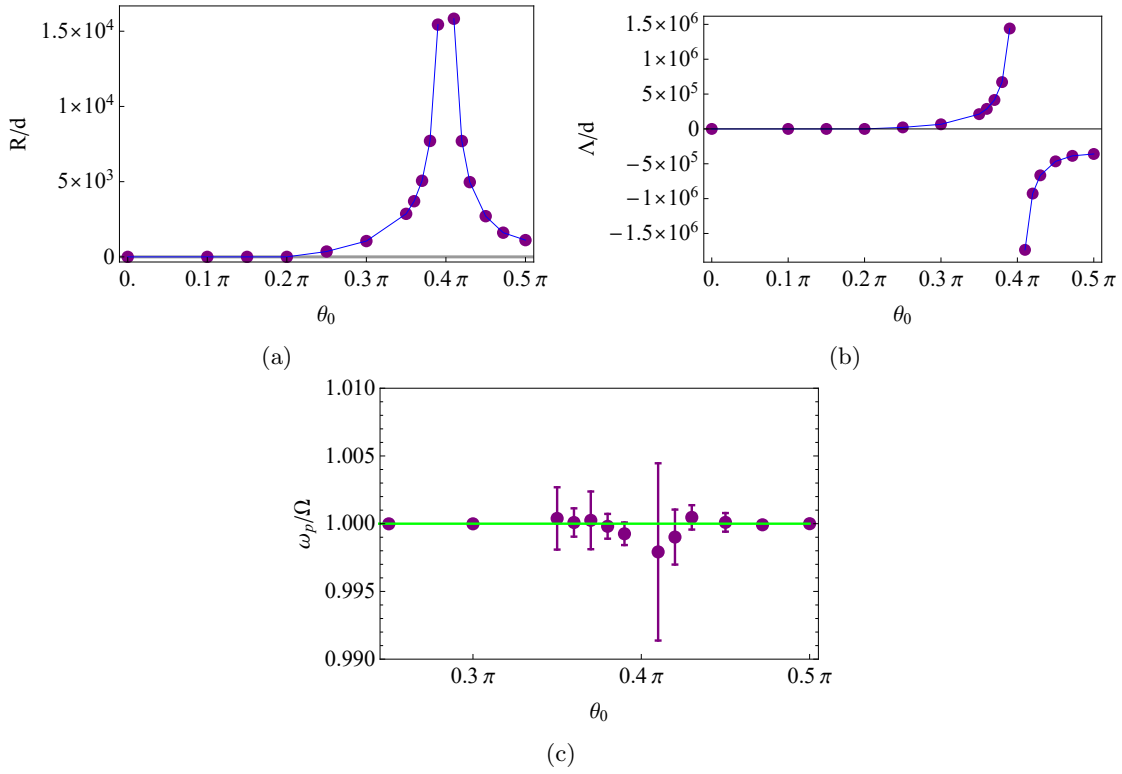

Figure 6.5: The behaviour of the helix as function of the starting orientation. (a) The trajectory radius R and (b) pitch Λ are shown as a function of the starting orientation angle θ_0. For $\theta_0 \leq 0.2\pi$, $R = \Lambda = 0$, then both increase until $\theta_0 = 0.4\pi$ where $R = \Lambda = \infty$ (c) The ratio of the angular velocities of the precession of the helix, ω_p, and the helical trajectory, Ω, are plotted as a function of the starting orientation θ_0. Within the error bars $\omega_p/\Omega = 1$, thus those angular velocities are equal.

($\theta = 0.5\pi$). The results are shown in Figure 6.5. In Figs. 6.5a, 6.5b the radius R and the pitch Λ of the trajectory are plotted as a function of θ_0. For $0 \leq \theta_0 \leq 0.2\pi$ the helix orients itself horizontally. Then the center of mass moves parallel to gravity, while the helix rotates in the xy-plane, see Fig. 6.6a. For $0.25\pi \leq \theta_0 < 0.4\pi$ the helix rotates clockwise around the z-axis, while sedimenting, see Fig. 6.6b. The radius and pitch of the trajectory increase with θ_0. At $\theta_0 = 0.4\pi$, $R \to \infty, \Lambda \to \infty$; thus the helix moves in a diagonal path, as shown in Fig. 6.6d. This marks a transition point, since the direction of rotation changes and the radius and pitch decrease for increasing θ_0. The trajectory shown in Fig. 6.6c shows an example of this behaviour. Note, however, that we have chosen to show the trajectory obtained with other parameter settings, $w = 4, \theta_0 = 0.25\pi$ for clarity reasons.

We have studied the ratio of the precession frequency, ω_p, of the long axis of the helix. and the angular velocity of the center of mass, Ω. The results are shown in Fig. 6.5c. Within the error bars,

$\omega_p/\Omega = 1$, thus the frequencies are equal. This means that the angle of the long axis with the trajectory is fixed. Because the inertia terms are neglected, this is necessary to describe a circular path. The behaviour of the axis of the helices is further investigated in Fig. 6.7. The amplitude of the nutation, $\Delta\theta$, and the ratio of the spinning frequency, ω_s, and nutation frequency, ω_n, are plotted as a function of θ_0 in Fig. 6.7a. The amplitude of nutation decreases for increasing θ_0. The ratio $\omega_s/\omega_n \approx 1$. Thus, the frequency of the nutation is equal to the spinning frequency of the helix around its long axis, which means that they induce each other. All rotations and horizontal translations are induced by hydrodynamic friction. The nutation and spinning are caused by the same effect. If one of the axis of the helix changes, the flow field around the helix changes and therefore the other axis will change as well. For $|\theta_0| < 0.2\pi, \hat{\boldsymbol{\beta}} = (0, 0, 1)$, no nutation is observed. The amplitude $\Delta\theta$ decreases, when $\hat{\boldsymbol{\beta}}$ aligns more perpendicular to gravity. Nutation will induce spinning and vice-versa.

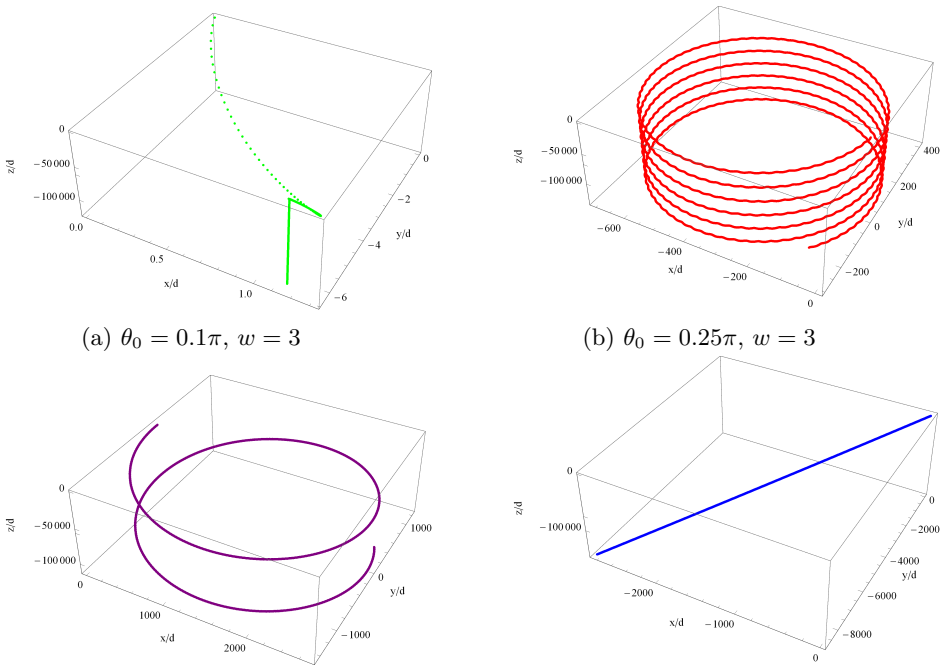

(a) $\theta_0 = 0.1\pi$, $w = 3$

(b) $\theta_0 = 0.25\pi$, $w = 3$

(c) $\theta_0 = 0.25\pi$, $w = 4$

(d) $\theta_0 = 0.4\pi$, $w = 3$

Figure 6.6: The trajectory of the center of mass for a sedimenting helix. The figures show the four observed trajectory styles. The parameter settings are $r/d = 2, \lambda/d = 3\pi$. (a) The helix orients itself horizontally and then drops down vertically. The helix rotates (b) clockwise, (c) anti-clockwise respectively around the z-axis while moving downwards describing a helical trajectory. For clarity, we have chosen to a higher winding number for (d). (d) The center of mass moves diagonally.

We have seen that the orientation of the helix around its long axis influences the flow field of the helix. It would therefore be interesting to investigate whether an initial rotation around the long axis would change the sedimentation behaviour.

6.1.4 Chirality

The difference in behaviour of a right- and left-handed helix, ($\lambda > 0$ and $\lambda < 0$, respectively) is investigated. The starting orientation is varied for a helix with parameter setting $r/d = 2, w = 3$ and $\lambda/d = \pm 3\pi$. The gravitational force is equal for all simulations. The results are shown in Table 6.2. The radius of the trajectory and the nutation amplitude $\Delta\theta$ are the same for both chiralities. The angular velocities of the precession and the spinning have opposing signs for the different chiralities. The absolute values are the same. Thus, the chirality only regulates the direction of motion. This is precisely what you would expect on the basis of geometry.

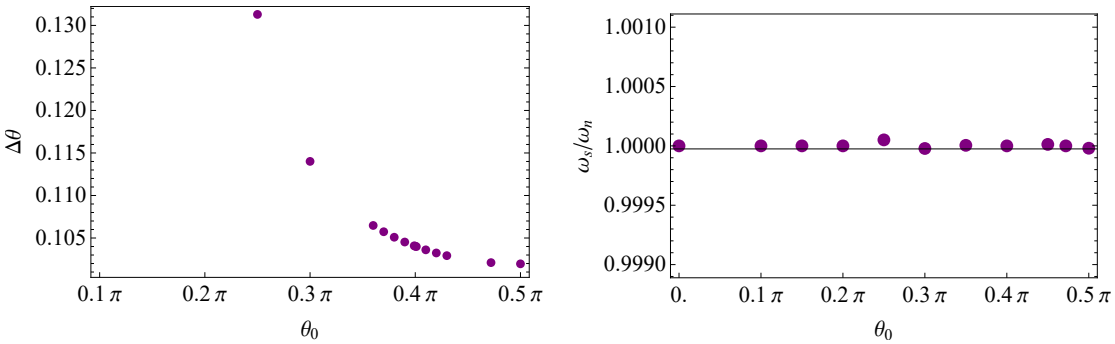

(a) (b)

Figure 6.7: The behaviour of the spanning axis of the helix as function of the starting orientation. (a) The amplitude of the nutation $\Delta\theta$ is plotted as function of the starting orientation angle θ_0. $\Delta\theta$ decreases for increasing θ_0. (b) The ratio of the spinning frequency and nutation frequency, ω_s/ω_n, is plotted as a function of the starting orientation. The ratio is for every angle ≈ 1, which means that the frequency of the nutation of the long axis and spinning of the helix around its long axis are equal.

	R/d		$\omega_p\tau$		$\omega_s\tau$		$\Delta\theta$	
θ_0 \ $\lambda/3\pi d$	-1	$+1$	-1	$+1$	-1	$+1$	-1	$+1$
0.2π	0	0	-0.0127	0.0127	0	0	0	0
0.3π	1050	1050	0.00066	-0.00066	0.177	-0.177	0.114	0.114
0.4π	∞	∞	0	0	0.231	-0.231	0.104	0.104
0.5π	1113.5	1113.5	-0.00013	0.00013	0.247	-0.247	0.102	0.102

Table 6.2: Influence of the chirality on distinctive parameters. The sign of λ defines the chirality, ω_p is the angular precession velocity of $\hat{\boldsymbol{\alpha}}$ around $\hat{z}$, ω_s the angular spinning velocity and $\Delta\theta$ the amplitude of nutation. The magnitudes of the parameters does not depend on the chirality, but the sign of the angular velocities are a function of the sign of λ. Thus, the chirality regulates the direction of motion.

6.1.5 Aspect ratio

We study the influence of the aspect ratio of the helix on the sedimentation trajectory. First by changing the aspect ratio of the winding itself, while keeping the number of windings fixed. Then, by changing the number of windings, whilst keeping the radius r and the pitch length λ of the helix fixed.

Pitch length

For $r/d < 4$ the radius r of the helix influences the results significantly given a fixed pitch-radius ratio λ/r, as shown in subsection 6.1.2. Therefore, we kept the radius r fixed, while varying λ/d between 1.2π and 8π to tune the aspect ratio described by the angle $\chi = \arctan 2\pi r/\lambda$. The results for $r/d = 3, w = 4, \theta_0 = 0.25\pi$ are shown in Fig. 6.8. The radius R and the pitch Λ of the trajectory decrease for increasing values of χ. Thus, a helix with a larger pitch describes a larger helical trajectory. A simple explanation could be that when the pitch length increases, the resemblance of the helix tends to look like a rod for which the sedimentation behaviour is a straight diagonal line.

Winding number

Another way to change the aspect ratio of the helix, is to change the number of windings. The parameter settings used are $r = 2, \lambda = 3\pi, \theta_0 = 0.25\pi$, the number of beads per winding is 12 except for $w = 6$, there the number is 11. The influence of the number of windings on the trajectory radius R and pitch Λ as well as the nutation is shown in Fig. 6.9. For $w = 1, 2$ there is no helical trajectory. The helix orients its long axis horizontal and sediments vertically. For more winding numbers, a helical trajectory is observed. However, from the graphs it is not clear how the trajectory depends on the number of

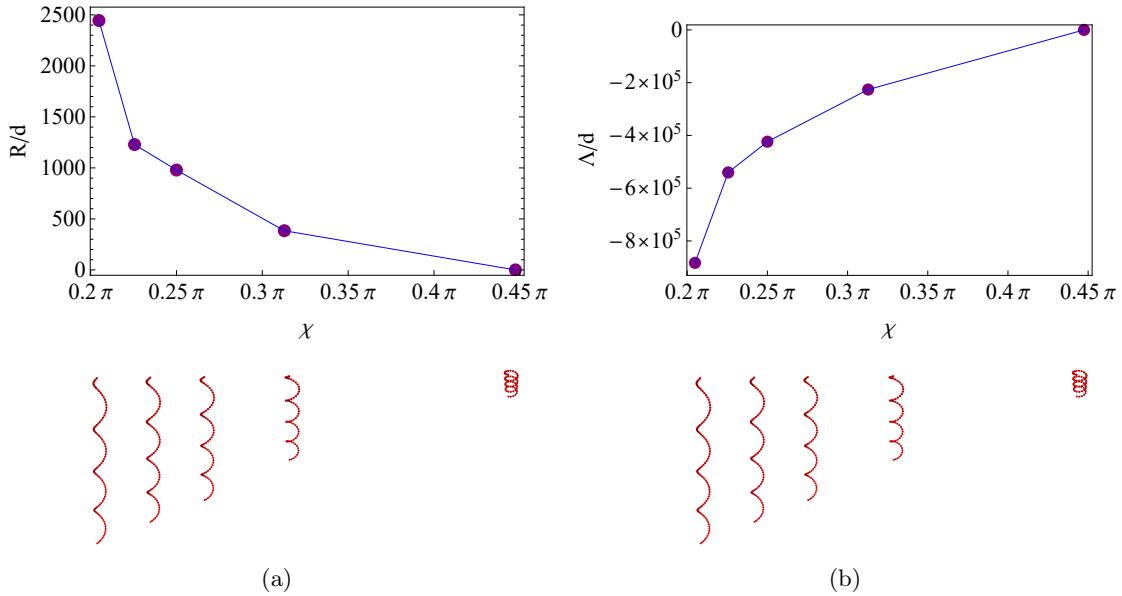

(a) (b)

Figure 6.8: The sedimentation behaviour as function of the angle χ. $\chi = \arctan 2\pi r/\lambda$ and indicates the aspect ratio of the winding of the helix. The corresponding helices are visualised below the horizontal axis. (a) The trajectory radius R and (b) pitch Λ are plotted as function of χ. R increases with increasing χ, while $\Lambda < 0$ decreases. Thus, a helix with a larger pitch length will have a larger helical trajectory. The helix has parameter settings $r = 3, w = 4, \theta_0 = 0.25\pi$, $\lambda > 0$ was varied to tune χ.

windings. The handedness of the trajectory even changes sign when w increases from 3 to 4. We would have expected both the radius and the pitch to increase with the winding number, since there is more friction, when the number of windings is increased.

In Fig. 6.9c the average orientation angle, $\langle\theta\rangle_t$ and the maximum and minimum angle are plotted as a function of the number of windings. The difference between $\langle\theta\rangle_t$ and θ_0 decreases for larger values of w, just as the difference between the extrema and the average, which defined the amplitude of the nutation. That the amplitude of the nutation decreases, could have been expected. We have seen in subsection 6.1.3 that the nutation is related to the spinning of the helix along its long axis. For an infinite number of windings, no nutation would be expected, because every rotation of the helix around its long axis would lead to the same physical situation. Therefore no nutation can occur. Thus, increasing the number of windings, decreases the hydrodynamic effect of a change in $\hat{\boldsymbol{\beta}}$.

The plots for R and Λ show that their values change, but how they depend on w is not clear from the figures. More measurements are needed, preferably for thinner helices, to draw conclusions on the effect of the winding number on the sedimentation radius and pitch. However, we can conclude that the long axis of the helix has a more stable angle with the z-axis for larger winding numbers.

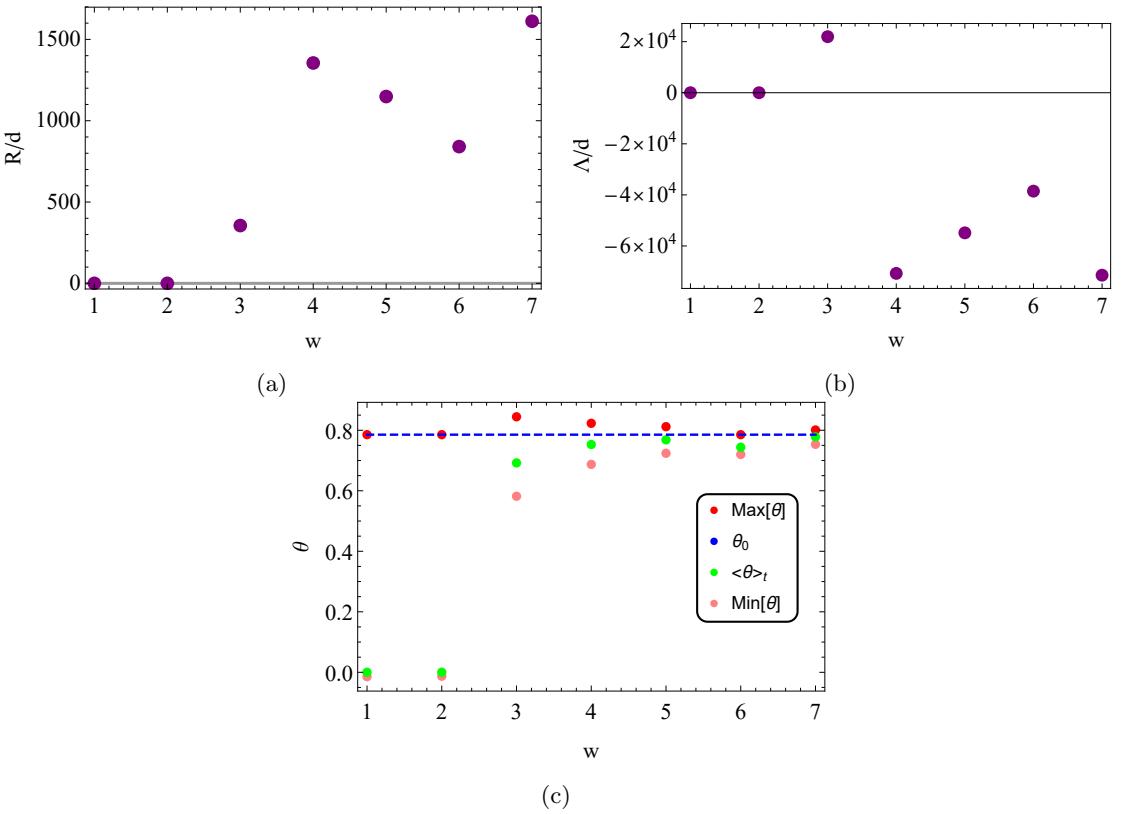

Figure 6.9: The effect of the number of windings on the sedimentation behaviour. (a) The radius R and (b) the pitch Λ are plotted as a function of the winding number w. R first increases until $w = 4$, then drops and increases again for $w = 7$. Λ changes sign at $w = 4$, thus the direction of the helical trajectory changes. (c) The maximum, Max$[\theta]$, minimum, Min$[\theta]$, and average orientation angle $\langle\theta\rangle_t$ are plotted as a function of w. The starting orientation θ_0 is indicated in blue. The deviation in θ decreases when the number of windings increases. The parameter settings used are $r = 2, \lambda = 3\pi, \theta_0 = 0.25\pi$

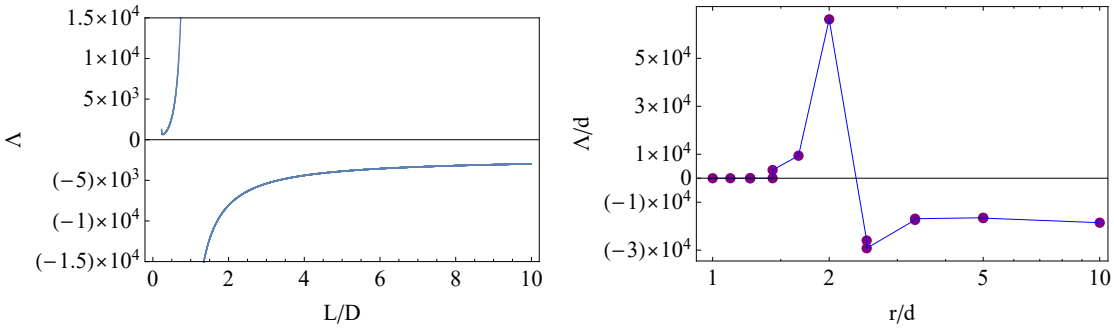

(a) Theory (b) RPY-method

Figure 6.10: The trajectory pitch length Λ as function of the thickness. (a) The theoretically calculated Λ is shown as function of the aspect ratio L/D, with L the length and D the diameter of the rod, which are used to theoretically model the helix. Lower values of L/D correspond to thicker helices. (b) The pitch length Λ obtained with the RPY method as function of the ratio r/d. The results display comparable behaviour as function of the thickness. The helix has parameter settings $\lambda/r = 1.5\pi, w = 3, \theta_0 = 0.25\pi$.

6.1.6 Comparison to theory

Now that we have fully described the results of our RPY simulation model, let us make the connection with the theoretical predictions by Dr. Morozov.

Thickness

Let us first consider the thickness of the helix. In the previous section we have seen that the simulation results indicate that this has a significant influence on the sedimentation behaviour. Recall the theoretical expressions from Chapter 4. R, Λ and Ω depend on γ, the ratio of the perpendicular and parallel friction coefficients. In the theoretical approximation it was assumed that the helix can be divided into small, thin, sphero-cylinders. The limit of the aspect ratio L/D, with L the length and D the diameter of the sphero-cylinder, was taken to infinity, and therefore $\gamma \to 2$. This approximation clearly does not hold for thick helices. When L/D decreases, γ will become smaller. We have shown the theoretical predicted behaviour of the trajectory pitch length Λ as function of the aspect ratio L/D in Fig. 6.10. For $L/D < 0.9$, Λ steeply increases with L/D and then changes sign for $L/D > 0.91$ where it behaves more gradually. This behaviour is similar to the simulation results as function of r/d, see Fig. 6.10b. But more simulation data are needed to draw definite conclusions on the quantitative behaviour of the helix as function of the thickness.

Starting Orientation

The theory predicts that the radius of the helical movement is zero for an initially horizontally and an initially vertically oriented helix, and maximum for a helix initially oriented at 45 degrees. The theory also predicts that the pitch Λ will increase with θ_0 and is maximal in $\theta_0 = 0.5\pi$. In our simulations we have seen that this is not the case for a helix with $r = 2, \lambda = 3\pi, w = 3$. Namely, we found that R and Λ asymptotically increase when the starting orientation $\theta_0 \to 0.4\pi$. The comparison can be seen in Fig. 6.11. The results are completely different, and we will discuss the possible sources next.

In our thickness measurements we have seen that the handedness of the helix changes when the thickness r/d changes from 2 to 2.5. We have seen that the deviation from the original orientation angle, θ_0, is larger for thicker helices. In the theory it is assumed that θ is fixed at its starting value. For the RPY results, this approximation does not hold. The fluctuation in θ has a significant effect on the behaviour. Because the nutation decreases for thinner helices, it could be interesting to compare the theory for different starting orientations with RPY simulation results for $r/d = 10$.

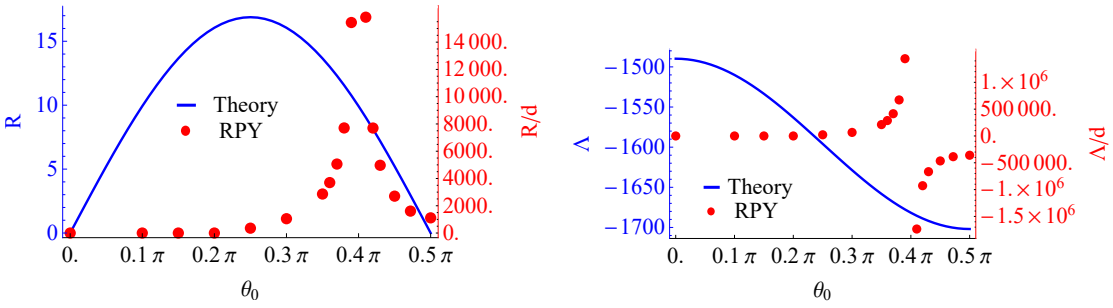

Figure 6.11: Comparison between the theoretical predicted dependency on the starting orientation and the results obtained by the RPY method. (a) The trajectory radius R and (b) the pitch Λ are plotted as function of θ_0. The theoretical calculated results are shown in blue, the results obtained by the RPY method in red. The theoretically calculated R is 0 when the helix is horizontally or vertically oriented and maximal for $\theta_0 = 0.25$ and is symmetric in this value. The theoretical Λ grows with θ_0. The results are not comparable to the results obtained with the RPY method. Calculations were made for $r = 2, \lambda = 3\pi, w = 3$.

Pitch length

The pitch length λ is varied between $1.2\pi - 8\pi$ for a helix with $r = 3, w = 4, \theta_0 = 0.25\pi$, to compare R and Λ with the results obtained by the RPY method. Note that we did these measurements in the regime where the helix is already thin $r/d > 2.5$. The results are shown in Fig. 6.12. R and Λ are displayed for different values of the angle $\chi = \arctan 2\pi r/\lambda$. χ describes the aspect ratio of a helical winding. The axis are scaled to compare both methods. Our results from the RPY-method show qualitatively comparable behaviour to the theory for $\chi < 1.1$. R decreases and $\Lambda < 0$ increases for increasing χ. This means that a helix with a smaller pitch length indeed has a smaller helical trajectory.

However, for $\chi > 1.1$ the theory still predicts a helical trajectory. The radius of this path will be small. With our RPY-method, we find that for $\chi = 1.4$ the helix will rotate to a horizontal position and then will sediment in a straight line. This, again, could be caused by the fluctuation in θ, which will allow the helix to rotate to its preferred orientation, which is not included in the theoretical approximation.

Winding number

The theory predicts that when the number of windings is increased, R and Λ grow, see Fig. 6.13. This means that when a helix has more windings, it will have a larger helical trajectory. This is expected,

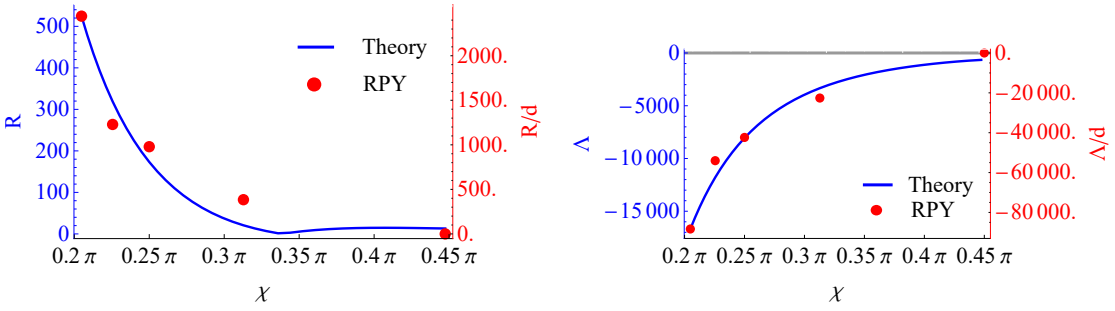

(a) (b)

Figure 6.12: Comparison of the results between the theoretical and RPY method for varying χ. The angle $\chi = \arctan 2\pi r/\lambda$ and indicates the aspect ratio of the helical winding. The simulation results are shown in red, the calculated results in blue. (a) The radius R and (b) the pitch Λ are plotted as function of χ. R decreases until $\chi \approx 1.1$ and stays small for larger χ. Λ decreases smoothly with χ. The results show a similar trend, except for $\chi = 0.45\pi$, where no helical trajectory occurs for the RPY method. The parameter settings of the helix were $r/d = 3, w = 4, \theta_0 = 0.25\pi$, λ was varied to tune χ.

since there is more friction with the fluid when the number of windings increases. We have seen that the RPY method shows no helical trajectory for $w = 1, 2$. For larger w a helical trajectory is found, with R increasing for $w = 3, 4$ and then an unclear (fluctuating) trend for greater w, see Fig. 6.13. Between $w = 3$ and $w = 4$ Λ even changes sign. Therefore the results are difficult to compare. For the RPY-method more measurements are needed for R and Λ, to draw any definite conclusions, preferably for higher r/d .

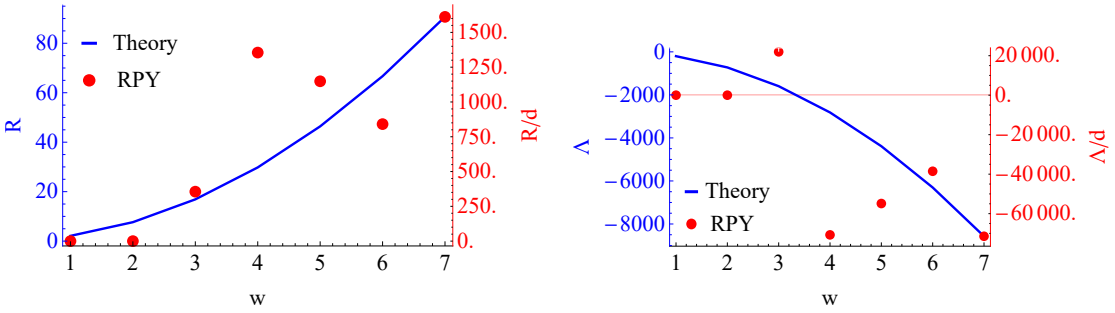

(a) (b)

Figure 6.13: The theoretical predicted dependency on the number of windings of the helix. (a) The trajectory radius R and (b) the pitch Λ are plotted as function of the number of windings w. Both increases with w. Thus a helix with more windings has a larger helical trajectory.

Since our results deviate for a number of parameter settings from the theoretically calculated behaviour, we also want to compare them with another method. Modification of the theory to include a fluctuating θ should also be considered for future investigation.

6.1.7 Comparison to Lattice-Boltzman Simulations

In the previous section, we found that there was only limited agreement between our RPY results and the theoretical predictions based on the model by Dr. Morozov. Therefore, we compared to another simulation technique, namely lattice-Boltzmann (LB), in order to validate our method.

For a helix with radius $r = 3$, pitch $\lambda = 1$ and 4 windings, the trajectory of the center of mass obtained from the RPY method is compared with results from an LB simulation. The trajectory of the center of mass is shown in Fig. 6.14. The movement of the helix initially has x-, y- and z-components,

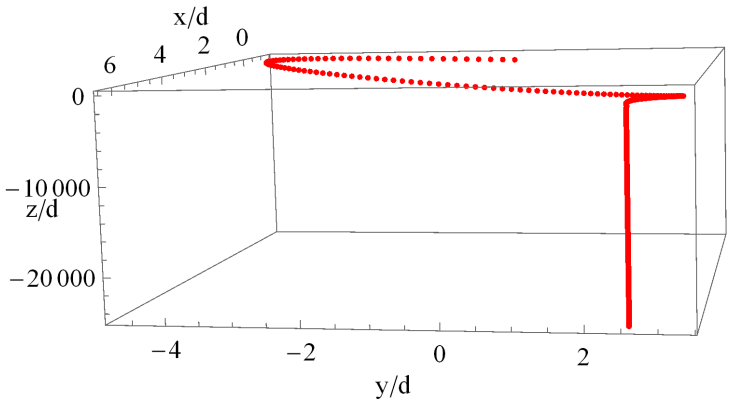

Figure 6.14: The center of mass trajectory of a helix with $r = 3$, $\lambda = 1$, 4 windings obtained from an LB simulation. After an initial period in which the velocity of has an x, y, and z component, the movement of the helix transitions into a vertical sedimentation.

but eventually transitions into a vertical sedimentation. The initial path is compared for both methods.

The x- and y-coordinate as a function of time are shown in Figs. 6.15a, 6.15b. The time of the LB simulations is scaled with a factor 1/57.6 to allow for comparison. This factor consists of two contributions: A factor of approximately 1/40 was expected because of the difference in force on the helix and the difference in time step for both methods. An extra factor of approximately 1.2^2 is obtained from the difference in bead size. A time-independent plot is shown in Fig. 6.15c.

The trajectories agree qualitatively, but difficulties in parameter matching (such as the bead diameter), prevented us from obtaining a quantitative match. The trend for the different starting angles is the same. Through this comparison, we are confident that the RPY-method predicts the right physical trends.

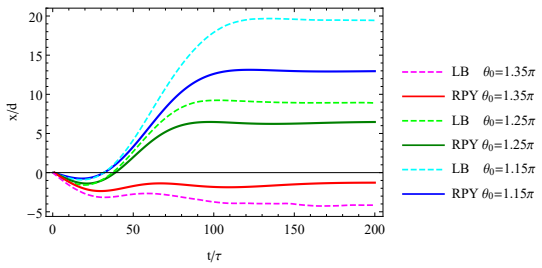

(a) xt-diagram

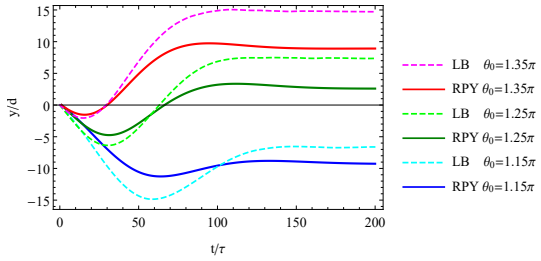

(b) yt-diagram

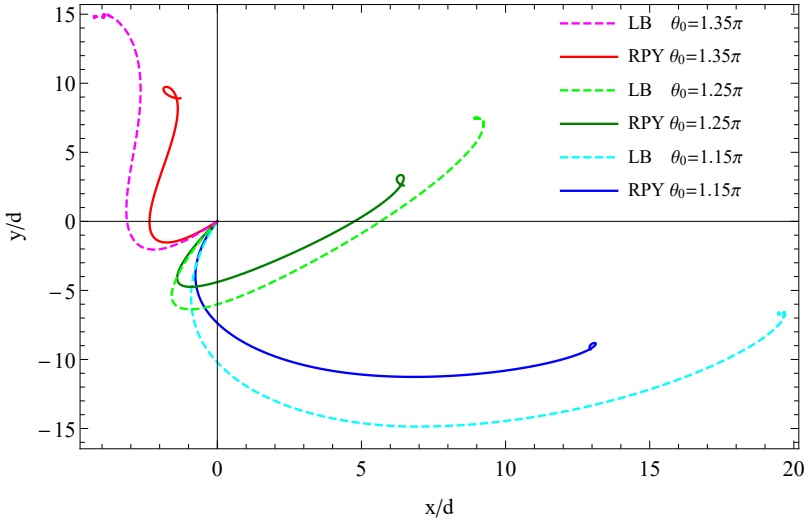

(c) xy-trajectory

Figure 6.15: Comparison between the trajectories obtained using the RPY and LB method for various starting angles θ_0. Diagrams for the center of mass of a helix with $r = 3, \lambda = 1, w = 4$ for the LB method (bright coloured, dotted lines) and RPY method (darker coloured, joined lines). We plot the x-component as a function of time in (a) and the y-component in (b). Time was scaled differently for the LB and RPY methods to facilitate comparison, see the text for an explanation. In (c) the trajectory is plotted in the xy-plane, which is independent of the time. The behaviour agrees qualitatively.

6.2 Two helices

Now that we have described the behaviour of a single helix and have convinced ourselves of the quality of our RPY method, let us turn our attention to the interaction between two helices. The helices have the following parameter settings: $r/d = 2,\ \lambda_1/d = \lambda_2 = 3\pi,\ w = 2$, with λ_1, λ_2 the pitch of helix 1 and helix 2 respectively. The initial angle θ_0 is equal for both helices. We have considered $\theta_0 = 0, \pi/2$. The initial distance, Δ_0, between the two centres of the helices is varied. $\Delta_0/d \in \{5, 6, 8, 10\}$, with d the bead diameter. For $\theta_0 = 0$, the distance is in the x-direction, for $\theta_0 = 0.5\pi$, the distance is in the y-direction. For $\theta_0 = 0.5\pi,\ \Delta_0/d = 6$, we have investigated how the trajectory depends on the chiralities of the two helices, the sign of λ_1 and $lambda_2$.

6.2.1 Vertically oriented helices

In Fig. 6.16 we have shown the trajectory of two initially vertically oriented helices, $\theta_0 = 0.5\pi$. Their initial distance is $\Delta_0/d = 10$. At $t = 0$, helix 1 is placed in the origin and helix 2 at $(0, 10, 0)$. The trajectories of the two helices in the xy-plane are almost overlapping, see Fig. 6.16a. In the xy-plane the trajectory of both helices is approximately equal. Note that their initial y-component is different, but that it is hardly visible, because of the length scale of the trajectory. From Fig. 6.16b we conclude that the distance between the two helices increases as function of time.

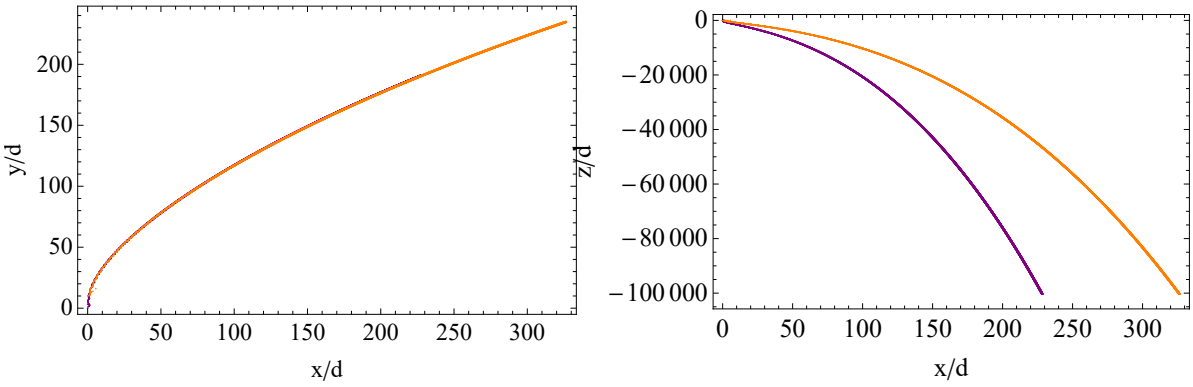

(a) xy-trajectory (b) xz-trajectory

Figure 6.16: Trajectory of two initially vertically oriented helices. The trajectory of the two helices is shown in (a) the xy-plane and (b) the xz-plane. At $t = 0$, helix 1 is placed in the origin and helix 2 at $(0, 10, 0)$. In the xy-plane the trajectory of both helices is approximately equal. Note that their initial y-component is different, but that it is hardly visible, because of the length scale of the trajectory. In the xz-plane the distance between the two helices increases as function of time. Their initial distance was $\Delta_0/d = 10$.

Before we study how the trajectory changes as a function of Δ_0, let us take a closer look at the trajectory of one of the helices. In Fig. 6.17, the initial trajectory of the first helix is displayed in the xy-plane and the xz-plane. In the xy-plane a clear periodic movement is observed while the x- and y-component increase as time processes. For the trajectory in the xz-plane the $z-$component decreases as a function of time and the x-component displays a periodic movement while x increases in time. Thus, the helix describes a rotational motion in the xy-plane while translating in the three dimensions. Let us define the radius of this periodic movement R and the angular velocity Ω. This periodic movement is difficult to see in Fig. 6.16, because the radius is small compared to the length of the entire trajectory.

Note that there are a couple of data points in both plots near the origin, which seem to be random points. These points are the coordinates in the first $t/\tau = 60$ time steps. To explain this behaviour we have shown the orientation angle θ for the first 225τ time steps in Fig. 6.18a. The helix is initially

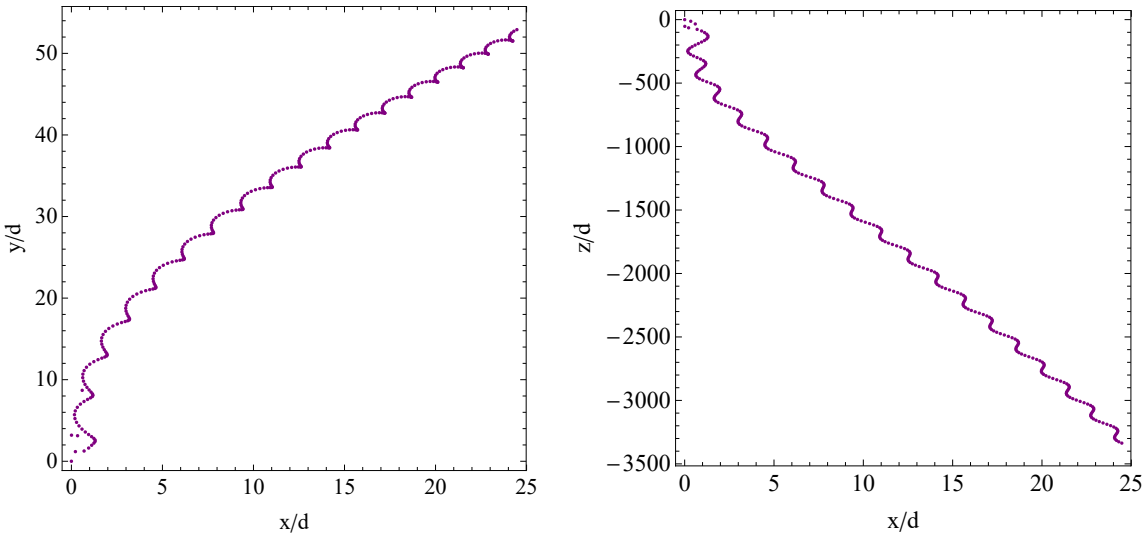

(a) xy-trajectory (b) xz-trajectory

Figure 6.17: Trajectory of one of the sedimenting helices for $\Delta_0/d = 10,\ \theta_0 = 0.5\pi$. The initial trajectory of the helix is shown in (a) the xy-plane and (b) the xz-plane. At $t = 0$ the helix is oriented in the origin. In the xy-plane a clear periodic movement is observed while the x- and y-component increase as time processes. For the trajectory in the xz-plane the $z-$component decreases as a function of time while the x-component displays a periodic movement while x increases in time.

oriented at $\theta_0 = 0.5\pi$. Within $t/\tau = 75$, θ decays to approximately -0.5π. From $t\tau = 75$, $\theta = -1.518$ and the long axis nutates around this value. The amplitude of the nutation decreases with time, which is shown in Fig. 6.18b. Thus, the long axis of the helix rotates to align with gravity and for the rest of the trajectory the helix nutates around this value.

In section 6.1 we have seen that the nutation and spinning of the helix have the same frequency. We are interested to see whether that equality still holds. Method (ii) of the analysis is used on the dataset of $\hat{\boldsymbol{\beta}}_x$ and $\hat{\boldsymbol{\alpha}}_z$ to determine the spinning and nutation frequency, respectively. We found that $\omega_n\tau = \omega_s\tau = -0.02564 \pm 0.00001$ for both helices. Thus, the nutation and spinning of the helix have indeed the same frequency. We also compare this frequency to the angular celocity of the trajectory, Ω. Ω is found by applying method (i) of the analysis on the dataset of the x-coordinate of both helices. We found that $\Omega\tau = \omega_n\tau = -0.02564 \pm 0.00001$. Thus, the angular velocity of the helical trajectory equals the spinning and nutation frequency. This behaviour is different from the behaviour of a single helix.

Initial distance

We have discussed the sedimentation behaviour of two initially vertically oriented helices at a distance of $\Delta_0 = 10$. Now we want to investigate how the trajectory changes when the initial distance is changed.

In Fig. 6.19a the trajectories of the center of mass of the system for different Δ_0 are plotted in the xy-plane. It can be seen that the initial trajectory is different: the rotation of the center of mass in the xy-plane depends on Δ_0. For $t >> 0$ the curvature of the trajectories seems to be comparable. In Fig. 6.19b we have zoomed in on the first 60τ time steps. The initial velocity is very high and the center of mass changes direction discontinuously. Then the behaviour smooths. The changes in direction are caused by a rotation of the long axis of the helices which align with gravity. To investigate the initial trajectory more precisely, the simulation results for the time steps in between should be considered.

For different values of the initial distance Δ_0, we have plotted the distance between a helix and the center of mass of the system as a function of time in Fig. 6.20. The distance increases with time. Initially the

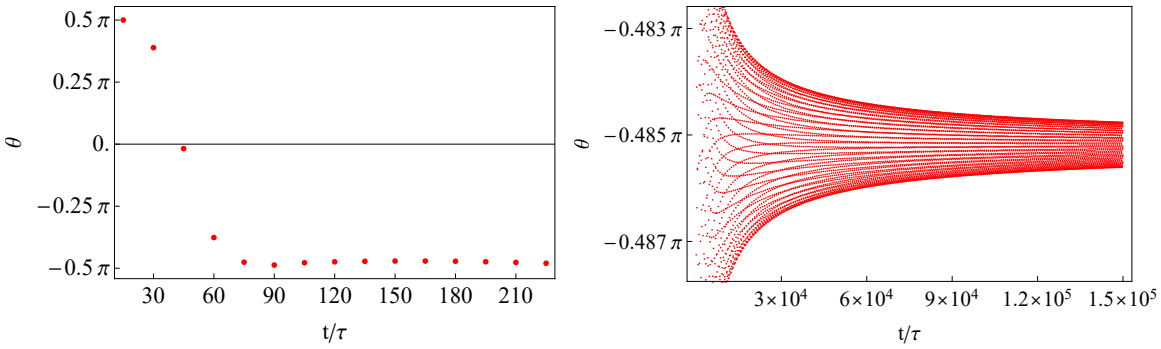

(a) (b)

Figure 6.18: The orientation angle θ as function of time. (a) θ is shown for the first $t/\tau = 225$. Within $t/\tau = 60$, θ decays from $\theta_0 = 0.5\pi$ to $\theta \approx -0.5\pi$. The helix orients its long axis parallel to the direction of gravity. (b) θ is shown as a function of time to indicate the amplitude of the nutation. The amplitude decreases with time.

change is very steep, but for $t/\tau > 1 \times 10^5$ the distance increases approximately linear with time. The trend is the same for all initial distances, but the quantitative values are slightly different. However, the dependency is not linear; the blue line displays the maximal distance, which corresponds to $\Delta_0/d = 10$, but the minimal line (purple) corresponds to $\Delta_0/d = 8$. Therefore, we cannot conclude how the distance depends on the initial distance.

In Fig. 6.16b we could see that there was a difference in z-component between the two helices. We have plotted the difference $(z_1 - z_2)/d$ as function of time for the different initial distances Δ_0/d, see Fig. 6.21. At first the sign and value of the difference in z-coordinate fluctuate as time develops. But then the difference tends to an average value around which it fluctuates. The average value depends on the initial distance. For increasing Δ_0/d, $(z_1 - z_2)/d$ increases, then drops for $\Delta_0/d = 10$. Therefore more measurements are needed to conclude on the trend of $(z_1 - z_2)/d$ as function of the initial distance. The average values lay between $6.5 - 9.5$ which is interesting if we compare this to the length of the helix: $L = w * \lambda = 6\pi \approx 18.8$. The difference in z-component is between $1/3L$ and $1/2L$.
We have investigated the frequency of the spinning, nutation and helical trajectory and found for all starting distances the same value, within the error: $\Omega\tau = \omega_s\tau = \omega_n\tau = -0.02564 \pm 0.0001$. Note that the angular velocity depends on the gravitational force, which was kept constant in these simulations.

Chirality

For $\Delta_0/d = 6$ we have investigated the influence of the chirality of the helices on the trajectory, which are defined by the signs of the pitches: λ_1 and λ_2. The trajectories of the center of mass are shown in Fig. 6.22. The direction of the trajectory depends on the chirality of helix 2, λ_2: For $\lambda_2 > 0$ the center of mass moves in the positive x-direction, for $\lambda_2 < 0$ in the negative x-direction. The sign of $\lambda_1\lambda_2$ determines the curvature of the trajectory. For $\lambda_1\lambda_2 > 0$ the center starts with a rotation of approximately 360° in the xy-plane, and after this rotation the path is curved. For $\lambda_1\lambda_2 < 0$ the center initially rotates approximately 180° and moves in a straight line afterwards.

The distance $\Delta/2d$ shows the same path as function of t/τ for all chirality combinations. Thus the distance does not depend on the chirality. However, the relative distance in z-component does depend on the chirality. For $\lambda_1\lambda_2 > 0$, $t/\tau >> 1$, $(z_1 - z_2)/d$ fluctuates between 9 and 9.1, for $q_1 = q_2 = -1$, between 8.8 and 8.9.

We have investigated the angular velocity of the trajectory. Ω changes sign if the chirality changes, and so do the spinning and nutation of the helix. This agrees with the results of section 6.1, in which we concluded that the chirality determines the direction of the rotation.

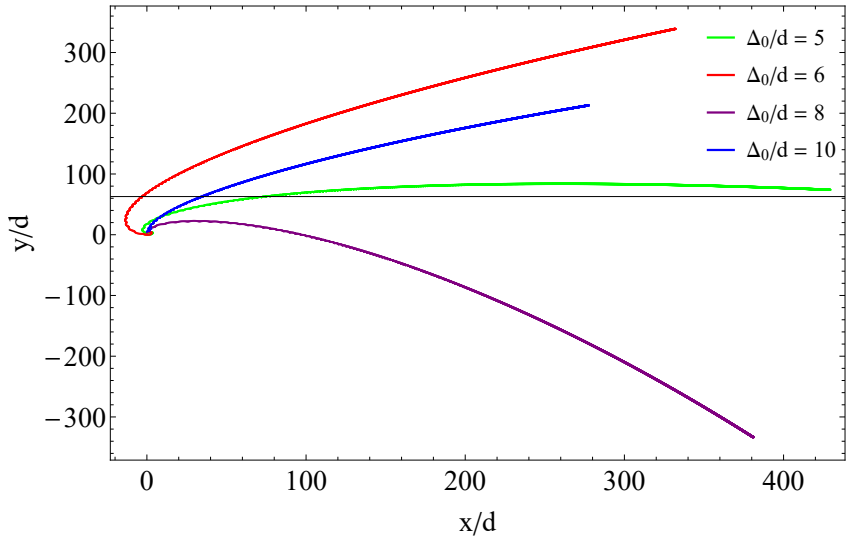

(a)

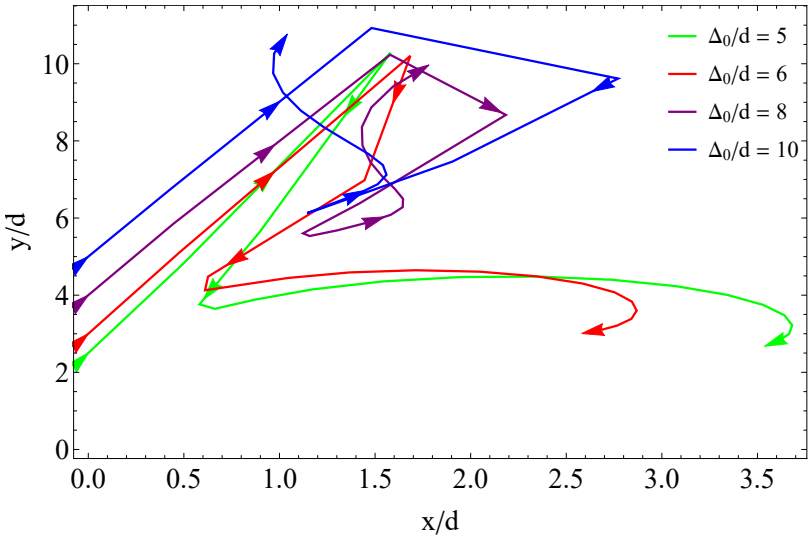

(b)

Figure 6.19: The sedimentation behaviour of two initially vertically oriented helices as function of their initial distance Δ_0/d. (a) The trajectory of the center of mass in the xy-plane is shown for different initial distances Δ_0. The initial trajectory depends on the distance and therefore the direction of movement. However, the curvature of the paths for $t >> 0$ seems to be comparable. (b) The behaviour of the center of mass for the first 60τ time steps. The direction of the trajectory is indicated by arrows. The initial velocity is very high and the center of mass changes direction discontinuously. Then the behaviour smooths.

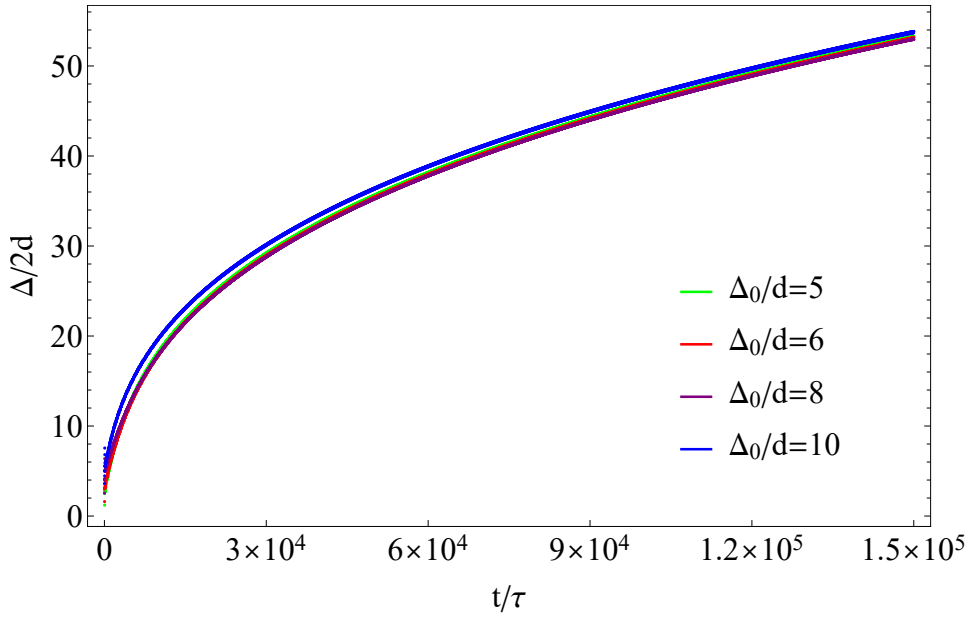

Figure 6.20: The change in distance between two initially vertically oriented helices for different initial distances. The distance between a helix and the center of mass of the system, $\Delta/2d$, is shown as a function of the time. The distance initially increases fast with time, but from $t/\tau \approx 6 \times 10^4$ $\Delta/2d$ scales approximately linear with time.

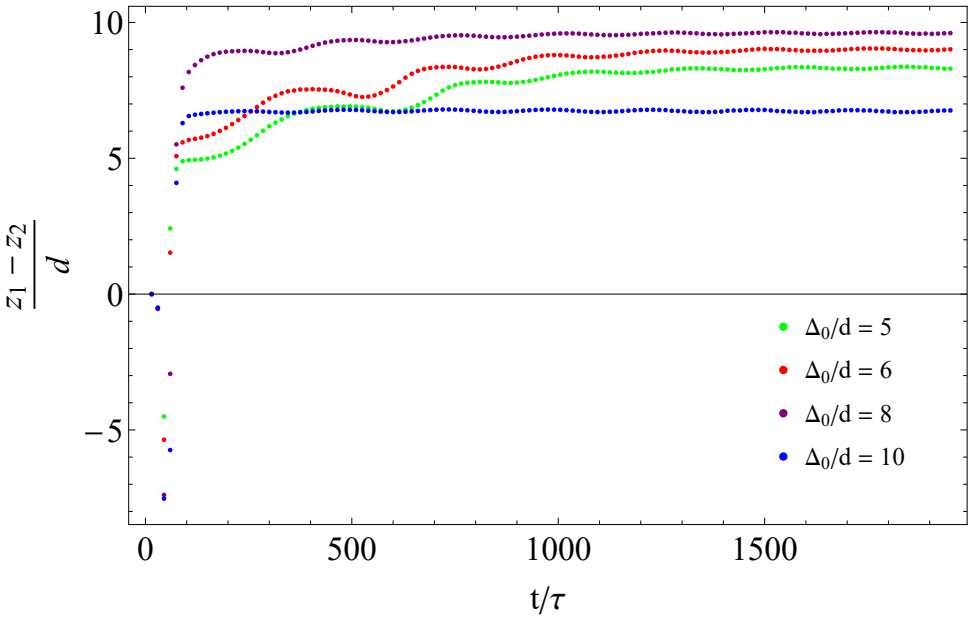

Figure 6.21: The relative difference in z-position for $\theta_0 = 0.5\pi$ in time for different initial distances. After an initial period of $t/\tau \approx 200$, the relative difference $(z_1 - z_2)/d$ tends to stabilise around a value which depends on the initial distance. For increasing Δ_0/d, $(z_1 - z_2)/d$ first increases, but the trend is broken for $\delta_0/d = 10$.

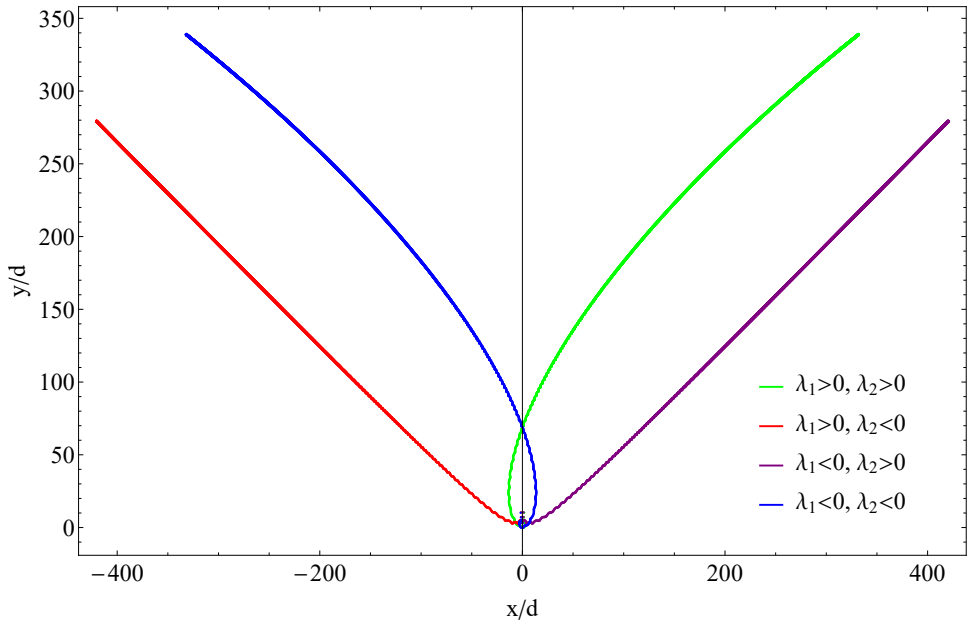

Figure 6.22: The xy-trajectory for the different combinations of chirality for two initially vertical oriented helices. The sign of λ_1, λ_2 indicate the chiralities of the two helices. The curvature of the path is larger for equal chiralities.

6.2.2 Horizontally oriented helices

In Fig. 6.23 we have shown the trajectory of two initially horizontally oriented helices. Their initial distance is $\Delta_0/d = 10$. At $t = 0$, helix 1 is placed in the origin and helix 2 at $(10, 0, 0)$. From Fig. 6.17a we see that the translational movement of the helices is rotated 180 degrees in the xy-plane. They move in opposite direction while rotating clockwise around that direction. The behaviour in the xz-plane seems symmetric in $x = 5$, see Fig. 6.23b. This is significantly different from the behaviour for two initially vertically oriented helices, see Fig. 6.16. There the trajectories in the xy-plane overlapped and the difference in z-component grew up to half the length of the helix. Thus the initial orientation does influence the trajectory of the two helices.

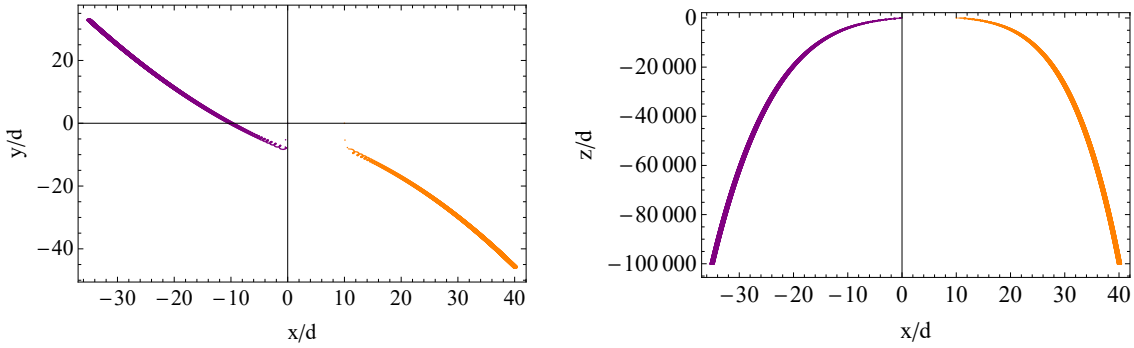

(a) xy-trajectory (b) xz-trajectory

Figure 6.23: Trajectory of two initially horizontally oriented helices. The trajectory of the two helices is shown. At $t = 0$, helix 1 is placed in the origin and helix 2 at $(10, 0, 0)$. (a) The helices move away from each other, the trajectory is rotated over 180 degrees in the xy-plane. (b) The distance between the two helices increases as well. The behaviour in the xz-plane seems symmetric in $x = 5$.

However, the behaviour of the long axis of the helix is the same: within $t/\tau = 60$, $\hat{\boldsymbol{\alpha}}$ almost aligns with the gravitational force: $\theta = -1.518$. The distance between the helix and the center of mass of the system, $\Delta/2d$, displays similar behaviour as well, see Fig. 6.24a. This is remarkable, as we have seen that the trajectories are qualitatively different. On the other hand, the orientation of the long axis of the helices after $t/\tau = 60$ is independent of the starting orientation. Therefore, the change in distance is expected to behave similarly.

The trajectories of the center of mass are plotted for the different initial distances in Fig. 6.24b. They rotate while moving in the xy-plane. The rotation is caused by the rotation of the two helices, which move in opposite direction. Their average coordinates therefore rotate as well. Because they move in opposite direction, the center of mass does not move very far away from the origin in the time period we considered.

The frequency of the rotation is equal to the frequency found for initially vertically oriented helices. We therefore think that the frequency is determined by the parameter settings of the helix.
When we consider the relative distance in z-component, something interesting happens. At first $(z_1 - z_2)/d$ behaves like a sinusoidal function, the amplitude of the fluctuation decays with time, see Fig. 6.25a. The average of the difference decreases with increasing Δ_0/d. However, at later times, there is no difference in average or amplitude between the different in initial distances, see Fig. 6.25b. $(z_1 - z_2)/d$ fluctuates between 0 and -0.10.

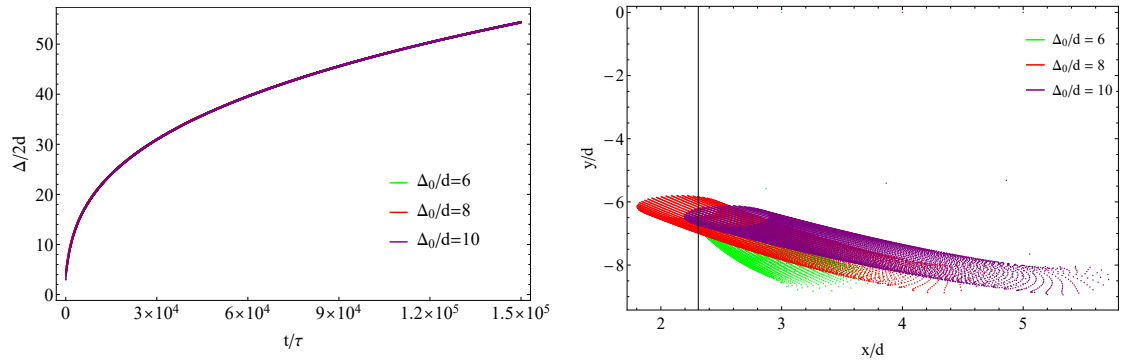

(a) (b)

Figure 6.24: Behaviour of two initially horizontally aligned helices. (a) The distance between a helix and its center of mass, $\Delta/2d$ is plotted as a function of time for the different Δ_0. The results overlap. (b) The trajectory of the center of mass of the system is plotted for the different initial distances. The results show a circular movement. The direction depends on the initial distance.

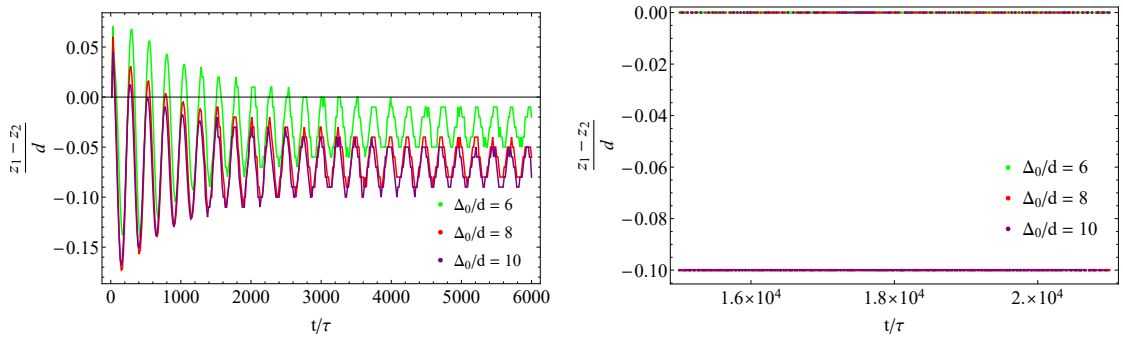

(a) (b)

Figure 6.25: The relative z-component as a function of time for $\theta_0 = 0$. The relative difference in z-component, $(z_1 - z_2)/d$ is plotted as a function of time for the different initial distances Δ_0/d. (a) Initially $(z_1 - z_2)/d$ behaves like a sinusoidal function, the amplitude of the fluctuation decays with time. The average of the difference decreases with increasing Δ_0/d. (b) At later times, there is no difference in average or amplitude between the different in initial distances. $(z_1 - z_2)/d$ fluctuates between 0 and -0.10.

6.2.3 Phase Shift

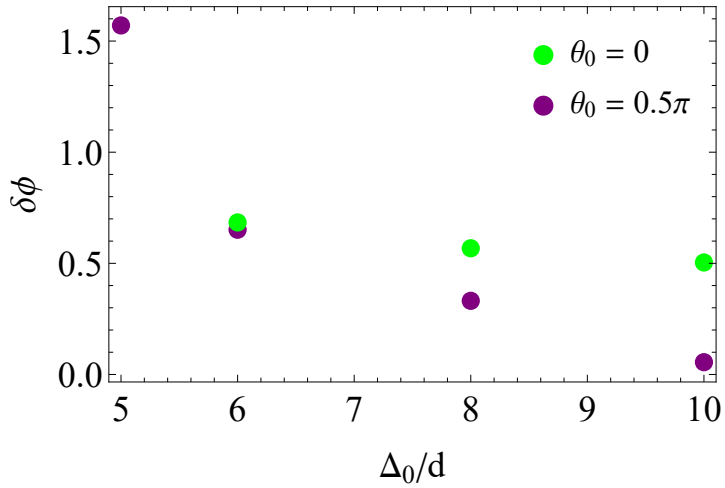

Figure 6.26: The shift in orientation $\delta\phi$ between the two helices as function of the distance Δ_0/d. The initially vertically oriented helices are displayed in purple, the horizontally oriented helices in green. The shift decreases as a function of the distance.

We have seen that the long axis of the helix orients itself almost parallel to gravity, independent of the initial conditions. Let us now look at the relative phase shift in $\hat{\boldsymbol{\beta}}$, $\delta\phi = |\phi_1 - \phi_2|$, which tells us how the helices are rotated around their long axis with respect to each other. The results for the initially horizontally and vertically oriented helices with varying distance are shown in Fig. 6.26. For the vertically oriented helices, the frequency shift decreases for increasing Δ_0. For $\Delta_0/d = 10$ the phase shift is 0.055. If the frequency shift is 0, this means that the helices are spinning in phase, a shift means that their rotation is out of phase. The decay in phase shift suggests that the helices will start to rotate in phase for large enough distances. However, more measurements are needed to draw a definite conclusion. The frequency shift for the initially horizontally oriented helices decreases as well, for larger values of Δ_0, but the slope of this behaviour is smaller. This is in agreement with the rest of our results, where we have seen that for $\theta_0 = 0$ the behaviour of the helices is less dependent on the initial distance, than for $\theta_0 = 0.5\pi$.

6.2.4 Conclusion

The above results show that a number of parameters such as the orientation of the long axis and the spinning frequency do not depend on the initial orientation or distance of the helices. For all the initial conditions we considered, the helices orient with their long axis almost along the negative z-axis, $\theta = -1.518$, and nutate around this value with a frequency of $\omega_n = 0.02564 \pm 0.00001$. The spinning frequency and angular velocity of the trajectory are equal to the nutation frequency. The flow field of the helices seems to stabilise the orientation of their long axes which almost align with the direction of gravity. We think that the angle between the gravitational force and the long axis causes a movement in the xy-plane. The rotational movement is caused by the nutation and spinning of the helices.

The chirality only influences the direction of the rotation, which is what you would expect on the basis of the results of a single helix. However, the initial distance and orientation do define the relative phase shift of the two helices. The trajectory of the center of mass is clearly dependent on the initial orientation. On the other hand, the initial distance between the two helices affects the beginning of their trajectory, and the relative distance in z, but it is not clear how it affects the trajectory for longer times. The simulation time should therefore be increased. For the initial trajectory, the data points in between should also be saved to determine the precise trajectory.

We have only investigated helices with two windings, due to limited time. It would be interesting to consider higher winding numbers. An initial phase shift in the orientation would be an interesting parameter to test as well. We have seen that the frequencies do not depend on the initial orientation or distance. We think these depend on the parameter settings of the helix. It would therefore be interesting to vary the radius and pitch of the helix, to determine whether the frequencies change.

Chapter 7

Conclusion

Summarising, in this thesis we have used the RPY method to study the sedimentation of rigid bodies consisting of spherical beads: of our main interest was the sedimentation of one and two helices. The method was verified for simple bodies (single sphere, two spheres, dumbbell, L-shape), which showed good agreement with literature. The results for a single helix were compared with theoretical calculations using slender-body theory, and lattice-Boltzmann simulations. For some of the parameters investigated, the results were completely different from the theoretical expressions. However, since the qualitative comparison to the results of the LB simulations was very well, we are confident that the RPY method predicts the right physical trends. Below we will discuss our main results and will give an outlook on the use of this method.

For the center of mass of a single helix we found four qualitatively different sedimentation trajectories:

- A vertical sedimentation trajectory after the helix has aligned its long axis with the xy-plane.
- A helical sedimentation trajectory of which the handedness was equal to the handedness of the helix.
- A diagonal trajectory: the center of mass moves in a straight line with an x-, y- and z-component.
- A helical sedimentation trajectory of which the handedness opposes the handedness of the helix.

For the single helix we observe three forms of rotation:

- Precession: The long axis of the helix will rotate in the xy-plane to fix its angle with the trajectory.
- Spinning: The helix rotates around its long axis.
- Nutation: The angle of the long axis with the xy-plane periodically fluctuates around an average value.

For a single helix we showed that the distance between the beads which we use to model the helix, converges when the beads approach each other. The nutation is not influenced by the differences in bead distance (except when it is very large), indicating that the observed nutation is not caused by the irregularities of the helix.

The thickness of the helix, r/a, strongly influences the sedimentation behaviour. For very thick helices, no helical trajectory is observed. The radius and pitch of the trajectory then strongly increase until the trend is broken and the handedness changes sign. We compared this to slender-body theory and found a qualitatively similar trend. The trend is explained by the change in friction components if the thickness increases. The ratio between the perpendicular and parallel friction coefficients us much smaller for thick helices than for thin helices. The deviation of the average orientation angle from the starting orientation and the amplitude of the nutation decrease when the helices get thinner. The fluid

friction is stronger for thick helices, which could explain this behaviour.

We found that the starting orientation angle of the long axis of the helix with the xy-plane has a big influence on the sedimentation trajectory. For helices which have an angle up to 0.2π their long axis rotates to align perpendicular to the gravitational force and the sedimentation trajectory is vertical. The long axis of the helix rotates in the xy-plane. When the starting angle θ_0 is increased, the radius and pitch of the helical trajectory increase up to ∞ for $\theta_0 = 0.4\pi$, while the helix spins around its long axis. The long axis precesses, such that the angle with the trajectory is kept constant, as was predicted by theory. For $\theta_0 = 0.4\pi$, the helix sediments diagonally, while spinning along its long axis. This marks a transition point, since the handedness of the trajectory changes and the radius and pitch start decreasing with increasing θ_0. The results do not agree with the theoretical prediction. One of the main reasons is that the theoretical approximation does not include deviations in θ. Another cause for the deviation could be that the helix we investigated is thick, while the theoretical approximation is based on very thin helices. We have seen that the thickness influences the results significantly.

The nutation and spinning of the axis have the same frequency, indicating that they induce each other. All rotations and horizontal translations are induced by hydrodynamic friction. The nutation and spinning are caused by the same effect. If one of the axis of the helix changes, the flow field around the helix changes and therefore the other axis will change as well. Thus, the orientation of the short axis, $\hat{\boldsymbol{\beta}}$, with respect to gravity influences the flow field of the helix. It would be interesting to test whether a difference in initial orientation in $\hat{\boldsymbol{\beta}}$ would affect the sedimentation trajectory. We have shown that the chirality of the helix, only changes the direction of the rotation, which is expected on the basis of geometry.

The aspect ratio of the helix was varied by changing the pitch and the number of windings. When the pitch length of the helix increases, the helical trajectory increases. In the limit of very large pitch lengths, the helix resembles a rod for which the sedimentation trajectory is diagonally, dependent on the initial orientation. The results show a similar trend to the theoretical predictions. For an increasing number of windings, we would have expected a larger helical trajectory, because there is more fluid friction. However, our data show indecisive trend. More simulations are needed, preferably for thinner helices, as those are more stable.

We have also verified some of the results to LB simulations performed by Dr. J. de Graaf. These agreed well qualitatively, although quantitative agreement was not obtained, because of difficulties in parameter matching. Through this comparison, we are confident that the RPY-method predicts the right physical trends.

We have seen that the theory not always predicts comparable results. It would be interesting to test whether the agreement improves if thinner helices are simulated. We suggest to include the time-dependency of θ in the theoretical approximation, as we have seen that it influences the sedimentation behaviour significantly.

For the sedimentation of two helices, we have investigated the behaviour as a function of the initial orientation, distance and chirality. We have shown that independent of the initial settings, the long axes almost align with the z-axis: $\theta = -1.518$, around which they nutate. The frequency of the nutation is independent on the initial settings, the chirality only changes the sign, analogous to the results for a single helix. The trajectories depend on the initial orientation and chirality. For the initially vertically oriented helices a relative difference in z-component stabilises the trajectory, while for initially oriented helices, the difference is close to 0. The relative phase shift of the two helices is influenced by the orientation and distance as well. To understand the origin of the difference in behaviour, a closer look should be made at the initial trajectory. The time step for which the data are saved, should be decreased to visualise this. However, the distance between the two helices shows similar behaviour, as well as the rotational motion of the helices. The angular velocity of this motion is equal to the nutation and spinning frequency. This indicates that the flow field of the helices stabilise each other in an orientation almost parallel to gravity. The deviation from the vertical orientation, is probably caused by the asymmetry of the helix along its long axis. We have already seen for a single helix that the nutation and spinning in-

duce each other. The small component of the long axis in the xy-plane results in the rotational trajectory.

We have only investigated helices with two windings, due to limited time. As most flagella exist of at least three windings, it is interesting to consider higher winding numbers. An initial phase shift in the orientation would be an interesting parameter to test as well. We have seen that the frequencies do not depend on the initial orientation or distance. We think these depend on the parameter settings of the helix. It would therefore be interesting to vary the radius and pitch of the helix, to determine whether the frequencies change. For equal starting orientation, the helices align. What happens if the initial angle is not equal? Is the vertical position stable for all configurations, would be an interesting question to ask.

This method could easily be extended to study the sedimentation behaviour of other rigid particles, such as cone-shaped helices. The main advantage in comparison with the lattice-Boltzmann simulations is that it is faster and allows larger parameter space. The RPY method is not affected by boundary effects, because the simulation box is not bounded.

Bibliography

[1] J. F. Brady and G. Bossis, "Stokesian dynamics," *Annual review of fluid mechanics*, vol. 20, pp. 111–157, 1988.

[2] J. Dhont, *An Introduction to Dynamics of Colloids*. Studies in interface science, Elsevier, 1996.

[3] H. C. Berg and R. A. Anderson, "Bacteria swim by rotating their flagellar filaments," *Nature*, vol. 245, no. 5425, pp. 380–382, 1973.

[4] L. Turner, W. S. Ryu, and H. C. Berg, "Real-time imaging of fluorescent flagellar filaments," *Journal of bacteriology*, vol. 182, no. 10, pp. 2793–2801, 2000.

[5] D. La Torre, J. Garcia, and V. A. Bloomfield, "Hydrodynamic properties of macromolecular complexes. i. translation," *Biopolymers*, vol. 16, no. 8, pp. 1747–1763, 1977.

[6] C. Brennen and H. Winet, "Fluid mechanics of propulsion by cilia and flagella," *Annual Review of Fluid Mechanics*, vol. 9, no. 1, pp. 339–398, 1977.

[7] E. M. Purcell, "The efficiency of propulsion by a rotating flagellum," *Proceedings of the National Academy of Sciences*, vol. 94, no. 21, pp. 11307–11311, 1997.

[8] L. Zhang, J. J. Abbott, L. Dong, K. E. Peyer, B. E. Kratochvil, H. Zhang, C. Bergeles, and B. J. Nelson, "Characterizing the swimming properties of artificial bacterial flagella," *Nano letters*, vol. 9, no. 10, pp. 3663–3667, 2009.

[9] S. E. Spagnolie and E. Lauga, "Comparative hydrodynamics of bacterial polymorphism," *Physical review letters*, vol. 106, no. 5, p. 058103, 2011.

[10] B. Rodenborn, C.-H. Chen, H. L. Swinney, B. Liu, and H. Zhang, "Propulsion of microorganisms by a helical flagellum," *Proceedings of the National Academy of Sciences*, vol. 110, no. 5, pp. E338–E347, 2013.

[11] R. M. Macnab, "Bacterial flagella rotating in bundles: a study in helical geometry," *Proceedings of the National Academy of Sciences*, vol. 74, no. 1, pp. 221–225, 1977.

[12] M. Kim, J. C. Bird, A. J. Van Parys, K. S. Breuer, and T. R. Powers, "A macroscopic scale model of bacterial flagellar bundling," *Proceedings of the National Academy of Sciences*, vol. 100, no. 26, pp. 15481–15485, 2003.

[13] M. Reichert and H. Stark, "Synchronization of rotating helices by hydrodynamic interactions," *The European Physical Journal E*, vol. 17, no. 4, pp. 493–500, 2005.

[14] C. W. Oseen, *Über die stoke'sche formel und über eine verwandte aufgabe in der hydrodynamik*. Almqvist & Wiksell, 1911.

[15] J. Rotne and S. Prager, "Variational treatment of hydrodynamic interaction in polymers," *The Journal of Chemical Physics*, vol. 50, no. 11, pp. 4831–4837, 1969.

[16] H. Yamakawa, "Transport properties of polymer chains in dilute solution: hydrodynamic interaction," *The Journal of Chemical Physics*, vol. 53, no. 1, pp. 436–443, 1970.

[17] E. Wajnryb, K. A. Mizerski, P. J. Zuk, and P. Szymczak, "Generalization of the rotnepragerya-makawa mobility and shear disturbance tensors," *Journal of Fluid Mechanics*, vol. 731, 9 2013.

[18] L. P. Fischer, T. Peter, C. Holm, and J. de Graaf, "The raspberry model for hydrodynamic interactions revisited. i. periodic arrays of spheres and dumbbells," *The Journal of chemical physics*, vol. 143, no. 8, p. 084107, 2015.

[19] M. Reichert, *Hydrodynamic Interactions in Colloidal and Biological Systems*. PhD thesis, University of Konstanz, 2006.

[20] G. K. Batchelor, *An Introduction to Fluid Dynamics*. Cambridge University Press, 2000. Cambridge Books Online.

[21] M. Lisicki, "Hydrodynamic interactions and wall drag effect in colloidal suspensions and soft matter systems," March 2014. Accessed: 2016-07-04.

[22] L. Durlofsky, J. F. Brady, and G. Bossis, "Dynamic simulation of hydrodynamically interacting particles," *Journal of Fluid Mechanics*, vol. 180, pp. 21–49, 7 1987.

[23] K. Hinsen, "Hydrolib: a library for the evaluation of hydrodynamic interactions in colloidal suspensions," *Computer Physics Communications*, vol. 88, no. 23, pp. 327 – 340, 1995.

[24] C. Sanderson, "Armadillo: An open source c++ linear algebra library for fast prototyping and computationally intensive experiments.," tech. rep., NICTA, 2010.

[25] A. George and J. W. Liu, *Computer Solution of Large Sparse Positive Definite*. Prentice Hall Professional Technical Reference, 1981.

[26] W. H. Press, S. Teukolsky, W. Vetterling, and B. Flannery, *Numerical Recipes in C: the art of scientific computing, Second Edition*. Cambridge Univ. Press, New York, 1992.

[27] J. G. de la Torre, G. del Rio Echenique, , and A. Ortega, "Improved calculation of rotational diffusion and intrinsic viscosity of bead models for macromolecules and nanoparticles," *The Journal of Physical Chemistry B*, vol. 111, no. 5, pp. 955–961, 2007.

[28] B. Ten Hagen, F. Kümmel, R. Wittkowski, D. Takagi, H. Löwen, and C. Bechinger, "Gravitaxis of asymmetric self-propelled colloidal particles," *Nature communications*, vol. 5, 2014.

[29] G. Batchelor, "Brownian diffusion of particles with hydrodynamic interaction," *Journal of Fluid Mechanics*, vol. 74, no. 01, pp. 1–29, 1976.

[30] M. M. Tirado, C. L. Martnez, and J. G. de la Torre, "Comparison of theories for the translational and rotational diffusion coefficients of rodlike macromolecules. application to short dna fragments," *The Journal of Chemical Physics*, vol. 81, no. 4, pp. 2047–2052, 1984.

[31] H. Löwen, "Anisotropic self-diffusion in colloidal nematic phases," *Physical Review E*, vol. 59, no. 2, p. 1989, 1999.

[32] H. J. Limbach, A. Arnold, B. A. Mann, and C. Holm, "ESPResSo – an extensible simulation package for research on soft matter systems," *Comp. Phys. Comm.*, vol. 174, pp. 704–727, May 2006.

[33] H. Binous, "Stokesian dynamic simulation of sedimenting spheres in a newtonian fluid," September 2005. Accessed: 2016-02-02.

Chapter 8

Acknowledgements

First of all I would like to thank my supervisor from Utrecht University, Prof. dr. Marjolein Dijkstra, for supervising me and giving me the opportunity to do part of my master project at another university. I enjoyed the experience of learning from both groups and comparing the similarities and differences. Then I would really like to thank Dr. Joost de Graaf from Edinburgh University for agreeing upon supervising me and for the time and energy spend on the supervision during the time I was there and afterwards in the writing process. I like to think I have learnt a lot about how research actually is done and how to write it down such that other people understand the results as well.
Thanks to Dr. Alexander Morozov from Edinburgh University for performing the theoretical calculations, which were an important contribution this project. And to Laura Fillion, who enabled me to run my simulations on the cluster and who I could ask for help on numerous things.

Both in Utrecht University as in Edinburgh University I was extremely lucky with the people I shared an office room with. I would like to thank all the master students from Utrecht for their help with Latex, Mathematica, coding or otherwise computer related problems, as well as their company and support. So thank you, Robin, Albert, Marjolein, Gideon, Maarten, Tom, Joep and Mayke!
I am extremely grateful to the warm welcome I received in Edinburgh from all the PhD-students in Physics, the shared lunches, pub evenings, occasional badminton play and the other activities in which I naturally could participate. An explicit thanks to the people I shared an office with, and who again helped me with computer, physics or other questions and always took the time to listen to me. So thank you, Laura, Alex, Tom, Chay, James and Steven. And finally thanks to all the people I bothered with questions, complains, or chapters to read, my lovely friends and family who were always willing to give advice and support, food or distraction. Special thanks to Aleid, who I bothered with questions by far the most.